# Should I stay or should I go? Spatio-temporal dynamics of Pseudomonas aeruginosa biofilms in microchannel flows

Massinissa Benbelkacem, Gabriel Ramos, Fatima El Garah, Yara Abidine, Christine Roques, Yohan Davit

# Should I stay or should I go? Spatio-temporal dynamics of bacterial biofilms in confined flows

**Massinissa Benbelkacem**[1,2], **Gabriel Ramos**[1,2], **Fatima El Garah**[2], **Yara Abidine**[1], **Christine Roques**[2], **Yohan Davit**[1*]

***For correspondence:**
yohan.davit@imft.fr (Yohan Davit)

[1]Institut de Mécanique des Fluides (IMFT), Université de Toulouse, CNRS, INPT, UPS, Toulouse, France; [2]Laboratoire de Génie Chimique (LGC), Université de Toulouse, CNRS, INPT, UPS, Toulouse, France

**Abstract** The vast majority of bacteria live in sessile biofilms that colonize the channels, pores and crevices of confined structures. Flow in these structures carries the nutrients necessary for growth, but also generates stresses and detachment from surfaces. Conversely, bacteria tend to occupy a large part of the available space and, in so doing, increase resistance to flow and modify transport properties. Although the importance of advective transport and hydrodynamic forces on bacteria is well known, the complex feedback effects that control development in confined geometries are much less understood. Here, we study how couplings between flow and bacterial development control the spatio-temporal dynamics of *Pseudomonas aeruginosa* in microchannel flows. We demonstrate that nutrient limitation drives the longitudinal distribution of biomass, while a competition between growth and flow-induced detachment controls the maximum clogging and the temporal dynamics. We find that successive cycles of sloughing and growth cause persistent fluctuations of the hydraulic resistance and prevent the system from ever reaching a true steady-state. Our results indicate that these self-sustained fluctuations are a signature effect of biofilm development in confined flows and could thus be a key component of the spreading of biofilms in infections, environmental processes and engineering applications. Consistent with the description of other bursting events, such as earthquakes or avalanches, we further show that the dynamics of sloughing can be described as a jump stochastic process with a gamma distribution of interevent times. This stochastic modeling approach opens the way towards a new quantitative approach to the characterization of the apparent randomness and irreproducibility of biofilm experiments in such systems.

## Introduction

Fluid flow and transport phenomena control many aspects of the life of bacteria (***Krsmanovic et al., 2021***), from the motility of cells (***Busscher and van der Mei, 2006***; ***Rodesney et al., 2017***) to the morphology of biofilm colonies (***Wang et al., 2022***), and even ecological interactions within populations (***Battin et al., 2016***). As a testimony to the importance of flow, bacteria have evolved specific strategies adapted to their mechanical environment and the rheology of fluids around them (***Dufrêne and Persat, 2020***). Bacteria have also evolved mechanisms to detect gradients of nutrients or toxic substances and adapt their movement accordingly (***Sampedro et al., 2014***). Recent studies further suggest that bacteria have mechanosensing and rheosensing capabilities (***Dufrêne and Persat, 2020***). For example, *Pseudomonas aeruginosa* has been found to regulate the *fro* operon in

response to the shear rate (**Sanfilippo et al., 2019**). Shear also modifies the intracellular levels of cyclic-di-GMP in cells of *P. aeruginosa* attached to a surface, initiating a sessile phenotype (**Rodesney et al., 2017**).

Even in dense surface-associated colonies known as biofilms (**Costerton et al., 1995**; **Flemming et al., 2016**), where cells are partially isolated from the fluid by a matrix of self-produced extracellular polymeric substances (**Flemming and Wingender, 2010**), flow still plays a fundamental role (**Thomen et al., 2017**; **Rusconi et al., 2011**). The flow of a viscous fluid around the matrix generates forces that can induce detachment or remodel the biofilm (**Besemer et al., 2007**; **Stoodley et al., 1998**) – the matrix essentially behaves as a viscoelastic material (**Peterson et al., 2015**) and thus can flow in response to stress (**Gloag et al., 2020**). Furthermore, key solutes, such as oxygen or nutrients, are transported in the fluid before they can diffuse in the biofilm and be consumed. This can lead to complex couplings between advective transport by flow, diffusion in the fluid and in the biofilm, and uptake by the cells (**Taherzadeh et al., 2012**; **Picioreanu et al., 2000**). It has also been recently demonstrated that flow can generate spatial heterogeneities in the activation of quorum-sensing within populations, as a result of autoinducers being washed away by flow in zones at high Péclet number (**Kim et al., 2016**; **Emge et al., 2016**; **Mukherjee and Bassler, 2019**).

A vast majority of bacteria live in biofilms that colonize confined geometries (**Conrad and Poling-Skutvik, 2018**). In such systems, biofilms can occupy a large portion of the available space and thus severely restrict flow. This tends to generate a two-way coupling between biofilm growth and transport phenomena whereby flow and transport mediate the development of the biofilm, but in return the development of the biofilm also modifies flow and transport (**Rittmann, 1993**; **Taylor and Jaffé, 1990a**; **Taylor et al., 1990**; **Taylor and Jaffé, 1990b**,c; **Vandevivere and Baveye, 1992b**,a; **Stewart and Fogler, 2001**; **Telgmann et al., 2004**; **Drescher et al., 2013**). In porous media, for instance, **Kurz et al.** (**2022**) showed that a *Bacillus subtilis* biofilm can clog a large part of the pore space, leaving only few preferential flow channels where a competition between shear-induced detachment and growth drives intermittency and spontaneous pressure fluctuations. Such bioclogging is an important component of systems as diverse as bioreactors in the food industry (**Verran, 2002**), biofilters for wastewater processing (**Aslam et al., 2018**), pipe flow for water distribution (**Cowle et al., 2014**), heat exchangers (**García and Trueba, 2020**), catheters used in medicine (**Bixler and Bhushan, 2012**), soil bioremediation (**Singh et al., 2006**), enhanced oil recovery (**Sen, 2008**; **Kryachko, 2018**) or biobarriers (**Lennox and Ashe, 2009**). Understanding the fundamentals of biofilm growth and feedback mechanisms with flow is therefore a crucial step towards developing better approaches in health and engineering.

Here, we investigate the role of couplings between nutrient transport, growth and detachment on biofilm development in microchannel flows. To do so, we developed a microfluidic setup generating a constant flow rate in a microchannel where a *P. aeruginosa* PAO1 GFP biofilm develops. This microfluidic system is further combined with timelapse microscopy, cellular microbiology and mathematical modeling to study the interactions between biofilm and flow, in particular the dynamics and spatio-temporal fluctuations.

## Results

Our experimental approach is summarized in Fig 1. We inoculated cells of *P. aeruginosa* PAO1 GFP in a microchannel and then continuously flowed a culture medium at constant flow rate to observe biofilm development. In what follows, we first study the effects of nutrient limitation on the spatial distribution of biofilm. We then focus on regimes where nutrients are in excess and biofilm development is primarily driven by the interactions with flow to detail the role of flow-induced detachment on the maximum clogging reachable and the temporal dynamics.

### Nutrient limitation controls the longitudinal distribution of the biofilm

To assess the impact of nutrient limitation, we performed experiments at flow rates over several orders of magnitude ($Q = 2\times10^{-2}$, $2\times10^{-1}$, $2\times10^{0}$, and $2\times10^{+1}\,\mu L/min$) and therefore different total

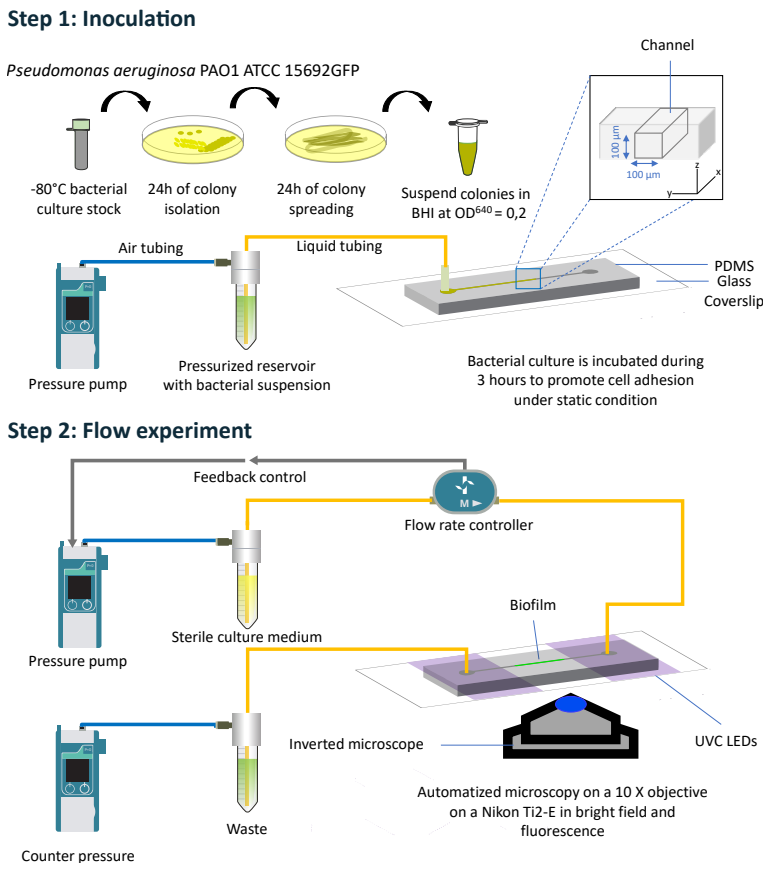


**Figure 1.** Schematic representation of the system and of the two main experimental steps. The first step is *P. aeruginosa* PAO1 GFP culture and inoculation in the microchannel (PDMS on glass, $100\ \mu m \times 100\ \mu m$ cross-section) using a pressure pump. The bacterial suspension is then left for 3 hours without flow to allow cells to adhere. The second step consists in flowing the culture medium at constant flow rate through the microchannel, while recording pressure fluctuations and imaging biofilm development via photonic microscopy. UVC radiation is used during the second step of the experiment to constrain the biofilm in a specific part of the channel.

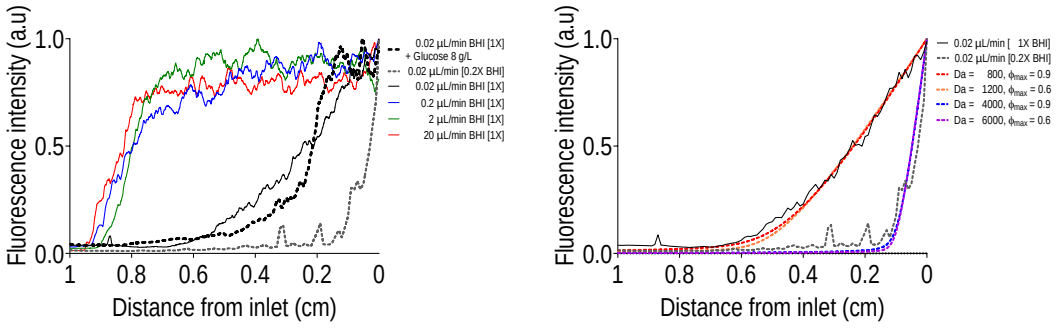


**(a)** Longitudinal distribution of fluorescence

**(b)** Simulations for $Q = 0.02\ \mu L/min$

**Figure 2.** Impact of nutrient limitation on the longitudinal distribution of biofilm. (a): Fluorescence intensity integrated for 72 hours for the flow rates $Q = 0.02\ \mu L/min$, $0.2\ \mu L/min$, $2\ \mu L/min$ and $20\ \mu L/min$ with 1× concentrated brain heart infusion (BHI) culture medium, along with $Q = 0.02\ \mu L/min$ with either 0.2×BHI or 1×BHI supplemented with $8\ g/L$ glucose. Nutrient limitation is observed only for $Q = 0.02\ \mu L/min$ and is strongly dependent upon the concentration of BHI components. (b): Simulations for $Q = 0.02\ \mu L/min$ for two values of $\phi_{\max}$ and the corresponding Damköhler numbers. The Damköhler numbers for the case with 0.2×BHI were simply obtained by multiplying those for the case 1×BHI by a factor 5. Each experimental curve in (a) and (b) is averaged over 3 replicates. In the model, we considered that the fluorescence signal is proportional to the product of biomass and concentration. We then integrated this signal in time and normalized it with the maximum value as $\overline{F}(x) = \int_0^t \phi(x,\tau)C(x,\tau)d\tau \Big/ \int_0^t \phi(x{=}0,\tau)C(x{=}0,\tau)d\tau$.

| Conditions | Variables | | | | | | |
|---|---|---|---|---|---|---|---|
| | $\sigma_0\ (Pa)$ | $\dot{\gamma}_0\ (s^{-1})$ | $Pe$ | $\phi_{\max}$ | $Da$ | $\tau_{\text{reac}}\ (s)$ | $Pe/Da$ |
| $Q = 0.02\ \mu L/min$ [BHI] = 0.2X | $2.4 \times 10^{-3}$ | $2.4 \times 10^{0}$ | $3.3 \times 10^{2}$ | 0.6 | $6 \times 10^{3}$ | 17 | $8.3\times10^{-2}$ |
| | | | | 0.9 | $4 \times 10^{3}$ | 25 | $5.5\times10^{-2}$ |
| $Q = 0.02\ \mu L/min$ [BHI] = 1X | | | | 0.6 | $1.2 \times 10^{3}$ | 83 | $4.2\times10^{-1}$ |
| | | | | 0.9 | $8 \times 10^{2}$ | 125 | $2.8\times10^{-1}$ |
| $Q = 0.2\ \mu L/min$ [BHI] = 1X | $2.4 \times 10^{-2}$ | $2.4 \times 10^{1}$ | $3.3 \times 10^{3}$ | 0.989 | $10^{3}$ | $\sim 100$ | $3.3 \times 10^{0}$ |
| $Q = 2\ \mu L/min$ [BHI] = 1X | $2.4 \times 10^{-1}$ | $2.4 \times 10^{2}$ | $3.3 \times 10^{4}$ | 0.968 | | | $3.3 \times 10^{1}$ |
| $Q = 20\ \mu L/min$ [BHI] = 1X | $2.4 \times 10^{0}$ | $2.4 \times 10^{3}$ | $3.3 \times 10^{5}$ | 0.907 | | | $3.3 \times 10^{2}$ |
| $Q = 200\ \mu L/min$ [BHI] = 1X | $2.4 \times 10^{1}$ | $2.4 \times 10^{4}$ | $3.3 \times 10^{6}$ | 0.786 | | | $3.3 \times 10^{3}$ |

**Table 1.** Summary of various quantities in the experiments and models. $\sigma_0$ is the shear stress in empty channel. $\dot{\gamma}_0$ is the corresponding shear rate. $D$ is an estimate diffusion coefficient for the limiting component. $Pe$ is the Péclet number. $\phi_{\max}$ is the maximum volumic fraction of biofilm. $Da$ is the Damköhler number. $\tau_{\text{reac}}$ is the reaction time. $Pe/Da$ is the ratio of Péclet to Damköhler numbers. To calculate dimensionless numbers, we used $D = 10^{-9}\ m^2 s^{-1}$ and $L = 10\ mm$.

fluxes of nutrients. Fig 2a shows the time-integrated distributions of the GFP fluorescence in the longitudinal direction for the different flow rates. We found that the active biomass expressing GFP is relatively uniform for flow rates between $0.2$ and $20 \mu L/min$ – the sharp decrease on the left-hand side at the outlet corresponds to the effect of the UVCs. For $0.02\ \mu L/min$, however, we observed a maximum value of the fluorescence intensity at the inlet on the right-hand side and a distinct decrease when moving towards the outlet.

Considering that the growth of *P. aeruginosa* PAO1 GFP is aerobic here – *P. aeruginosa* is a facultative anaerobe and can perform denitrification in anaerobic environments by anoxic respiration using nitrogenated compounds as final electron acceptors (***Arat et al., 2015***) but this produces less energy (***Bartberger et al., 2002***) – we hypothesized that this heterogeneity in biofilm development along the channel stems from a limitation of solute species required for growth, either oxygen or one of the nutrients in the growth medium. For the largest flow rates, advective transport through the channel should be fast compared to consumption, so that even bacteria at the outlet receive sufficient levels of nutrients and oxygen for biofilm development. For the lowest flow rate, however, one of the components introduced at the inlet is rapidly consumed by bacteria and becomes limiting, so that growth decreases with the distance from the inlet.

To better understand this limitation, we repeated experiments at $0.02\ \mu L/min$ either with BHI diluted $5$ times or by supplementing $1\times$BHI with additional glucose. Results in Fig 2a with the glucose supplementation show a similar longitudinal distribution of biofilm compared to assays without glucose, thus suggesting that this carbon source is not the limiting nutrient – it was confirmed by mass spectrometry that only a small fraction of the glucose was consumed. Results with the five times diluted BHI, however, show a much narrower window of biofilm growth, therefore suggesting that one of the components in the BHI is becoming limiting. Although oxygen probably features gradients within the biofilm (***Folsom et al., 2010***) and in the longitudinal direction, the inlet concentration of oxygen is identical for the two cases $1\times$BHI and $0.2\times$BHI, therefore indicating that oxygen is not the primary component limiting growth. Another factor that may further alleviate oxygen limitations is that PDMS is highly permeable to oxygen, so that there are in fact two sources of oxygen in our system: dissolved oxygen in the culture medium and oxygen coming from/through the PDMS.

To explore these different hypotheses and quantify the characteristic times of reactive transport, we simulated the development of the biofilm inside the channels, taking into account the couplings between biofilm growth and nutrient transport. The limiting nutrient is treated as a solute being transported by advection/diffusion and consumed by bacteria. We considered that mass

transport is much faster than bacterial growth and division, so that the problem is quasi-steady for solute transport (***Picioreanu et al., 2000***). The limiting nutrient was thus modeled as

$$\underbrace{Pe\partial_x C^\star}_{\text{Advection}} = \underbrace{\partial_{xx} C^\star}_{\text{Diffusion}} - \underbrace{Da\phi \frac{C^\star}{C^\star + K^\star}}_{\text{Nutrient uptake}}, \tag{1}$$

where $C^\star = \frac{C}{C_0}$ is the non-dimensionalized solute concentration with $C$ $\left[g \times m^{-3}\right]$ the concentration and $C_0$ $\left[g \times m^{-3}\right]$ the inlet concentration, $x$ is the longitudinal coordinate system normalized with the length of the channel $L = 10\ mm$, $\phi$ is the cross-section volume fraction of biofilm and $K$ $\left[g \times m^{-3}\right]$ the half-saturation constant. $Pe$ is the Péclet number defined as the ratio of longitudinal diffusion to advection times, $Pe = \frac{VL}{D}$ with $V$ $\left[m \times s^{-1}\right]$ the average velocity in the empty channel and $D$ an estimate diffusion coefficient of the solute – as a reference, for $D = 10^{-9} m^2 \times s^{-1}$, we have $Pe \simeq 330$ for $0.02\ \mu L/min$. $Da$ is the Damköhler number defined as the ratio of diffusive to reactive times, $Da = \frac{\alpha L^2}{C_0 D}$ with $\alpha$ $\left[g \times m^{-3} \times s^{-1}\right]$ the uptake rate. The term $\phi$ in the nutrient uptake indicates that consumption is proportional to the volume fraction of biofilm. Reference values are presented in Table 1.

For the biomass growth, we used a model capturing the coupled effects of growth and flow-induced removal,

$$\partial_t \phi = \underbrace{\frac{C^\star \left(1 + K^\star\right)}{C^\star + K^\star} \phi}_{\text{Growth}} - \underbrace{\mathcal{M} f(\phi) \phi}_{\text{Removal}}, \tag{2}$$

where $f(\phi) = \sqrt{\frac{\sigma}{\sigma_0}} = (1-\phi)^{-1}$ with $\sigma = \frac{A}{4} \frac{\mu Q}{h^3} (1-\phi)^{-2}$ the average tangential stress at the biofilm solid interface (see SI) and $\sigma_0 = \frac{A}{4} \frac{\mu Q}{h^3}$ the shear stress in the empty square cross-section channel (see Table 1 for reference values). Here $A$ is a scalar parameter characterizing the geometry of the cross-section colonization – $A = \frac{12}{1 - \sum_{n,\text{odd}}^{\infty} \frac{1}{n^5} \frac{192}{\pi^5} \tanh\left(n \frac{\pi}{2}\right)} \simeq \frac{12}{1 - 0.917 \times 0.63}$ (***Bruus, 2008***) if we consider a uniform layer of biofilm and only deal with square cross-sections. We also have $\mathcal{M} = \frac{\chi X}{Y \alpha \left(1 + K^\star\right)} \sqrt{\sigma_0}$, which is the dimensionless number characterizing the competition between growth and detachment, containing the rate of biomass detachment $\chi$ $\left[s^{-1} \times N^{-\frac{1}{2}} \times m\right]$.

A number of works express the detachment rate as proportional to the square root of the fluid shear stress at the biofilm fluid interface (***Coyte et al., 2017***). Here this could be written as $f(\phi) = \sqrt{\frac{\tau_{\text{shear}}}{\sigma_0}} = (1-\phi)^{-3/4}$ with $\tau_{\text{shear}}$ the shear stress at the biofilm fluid interface. Such approaches, however, were initially developed for flows in reactor systems where shear stress is dominant (***Duddu et al., 2009***; ***Rittman, 1982***) and neglect the contribution of the pressure stress to detachment ***Characklis et al.*** (***1982***), for instance, measured the rate of biofilm loss under different shear stresses generated by rotating the inner annulus of reactor at different speeds and found a linear relationship between biofilm loss rate and rotational speed. Upon clogging the microchannel, we expect the pressure difference to generate a significant force on the biofilm and to play an important role on detachment. We could have introduced a multi-modal form of detachment, with contributions from both the shear stress at the biofilm/fluid interface, scaling as $(1-\phi)^{-3/4}$, and the tangential component of the total stress at the biofilm/solid interface, scaling as $(1-\phi)^{-1}$. For simplicity, however, we consider a contribution of detachment scaling as $(1-\phi)^{-1}$.

Assuming that $\mathcal{M} \in ]0, 1]$, the model for the biomass can be written in a simpler form as

$$\partial_t \phi = \phi \left[ \frac{C^\star \left(1 + K^\star\right)}{C^\star + K^\star} - \frac{1 - \phi_{\text{max}}}{1 - \phi} \right], \tag{3}$$

with $\phi_{\text{max}}$ the maximum volume fraction of biofilm, defined as $\mathcal{M} = 1 - \phi_{\text{max}}$, $\phi_{\text{max}} \in [0, 1[$ and

$\phi \in [0, \phi_{\max}]$. The only non-trivial steady-state,

$$\phi_{\text{equ}} = 1 - (1 - \phi_{\max}) \frac{C^\star + K^\star}{C^\star (1 + K^\star)}, \tag{4}$$

reflects an equilibrium between the amount of biomass created and the amount of biomass detached. The trivial steady-state $\phi_{\text{equ}} = 0$ is stable when detachment exceeds growth, i.e. when $C^\star$ is lower than $\frac{K^\star(1-\phi_{\max})}{K^\star+\phi_{\max}}$. In assuming that $\mathcal{M} \in ]0, 1]$ and eliminating cases where $\mathcal{M} > 1$, we have not considered situations of systematic detachment $\phi_{\text{equ}} = 0$ for any value of the concentration, since this is not a situation that we encountered experimentally.

Fig 2(b) compares results of the model with those of the experimental fluorescence for the flow rate $0.02\ \mu L/min$ and $K^\star = 0.1$. To roughly assess the sensitivity of our simulation to uncertainties in the value of $\phi_{\max}$, we further considered two extreme values, $\phi_{\max} \simeq 0.6$ and $\phi_{\max} \simeq 0.9$. The model shows good agreement with experiments for $Da_{\text{BHI}\times 1} \simeq 1200$ in the case $\phi_{\max} \simeq 0.6$ and $Da_{\text{BHI}\times 1} \simeq 800$ in the case $\phi_{\max} \simeq 0.9$. The corresponding characteristic reaction time for nutrient uptake, $\tau_{\text{reac}} = {}^{C_0}/_{\alpha}$, ranges from $\simeq 83s$ to $\simeq 125s$. We further obtain an excellent correspondence between the model and the experimental data for the 5 times dilution of the BHI without any fitting, simply by multiplying the Damköhler number by a factor 5 – recall that, by definition, $Da = {}^{\alpha L^2}/_{C_0 D}$ with $C_0$ the inlet concentration so that dividing $C_0$ by 5 implies multiplying the Damköhler number by a factor 5. The fact that the behavior of the system with 5 times dilution of the BHI can be obtained without any fitting confirms that the primary limitation is indeed one of the components of the BHI, not oxygen.

With these estimations of characteristic times for uptake, we can also evaluate whether any form of radial limitation of nutrient is expected by comparing times for transverse diffusion and uptake. The characteristic time for diffusion in the radial direction is $\tau^h_{\text{diff}} = \frac{h^2}{D}$ with $h \simeq 50\ \mu m$ a characteristic length for the distance between the flow channel and the wall. Considering again a diffusion coefficient in the biofilm $D = 10^{-9} m^2/s$ for the limiting nutrient, we have $\tau^h_{\text{diff}} \simeq 2.5\ s$. Diffusive transport across the channel is therefore significantly faster than uptake, implying that there is no form of limitation in the transverse direction. In the spirit of the dimensional analysis performed for longitudinal transport, this can also be formalized as a radial Damköhler number, $Da_{\text{radial}} = {}^{\tau^h_{\text{diff}}}/_{\tau_{\text{reac}}} < 1$.

The complete picture for nutrient transport is therefore as follows. In the longitudinal direction, the distribution of biomass is driven by a competition between advective transport and reaction. This can be quantified using the ratio of the Péclet and Damköhler numbers, ${}^{Pe}/_{Da}$. When advective transport is faster than uptake, ${}^{Pe}/_{Da} > 1$, the distribution of the biofilm is uniform. On the other hand, when ${}^{Pe}/_{Da} < 1$, uptake is faster than advective transport so that growth is nutrient limited. Table 1 summarizes the values of ${}^{Pe}/_{Da}$ for the different cases and shows that the regime ${}^{Pe}/_{Da} < 1$ is reached only for the flow rate $0.02\ \mu L/min$. In the transverse direction, there is no nutrient limitation and the amount of biomass is determined by an equilibrium between growth and flow-induced detachment. The details of this mechanisms, and its impact on the temporal dynamics, is the core of the following sections.

## Hydrodynamic stresses affect all stages of development

We now focus on the flow rates $Q = 0.2$, 2 and $20\ \mu L/min$ that featured no strong nutrient limitation and thus allowed us to separate the effects of molecular transport from that of hydrodynamic stresses. We describe the temporal dynamics through two classes of measurements: the time evolution of the pressure and timelapse microscopy imaging. The evolution of the pressure was monitored in the inlet reservoir, while imposing a constant flow rate. From this measurement, we reconstructed the evolution in time of the hydraulic resistance of the zone of interest in the channel, $\mathcal{R}(t)$, where biofilm developed (see Material and Methods). This allowed us to determine the dynamics of the ratio $\frac{\mathcal{R}}{\mathcal{R}_0}$, with $\mathcal{R}_0$ the hydraulic resistance of the empty channel, as shown in Fig 3 (see also supplementary information figures S5, S8 and S11) and to analyze the different

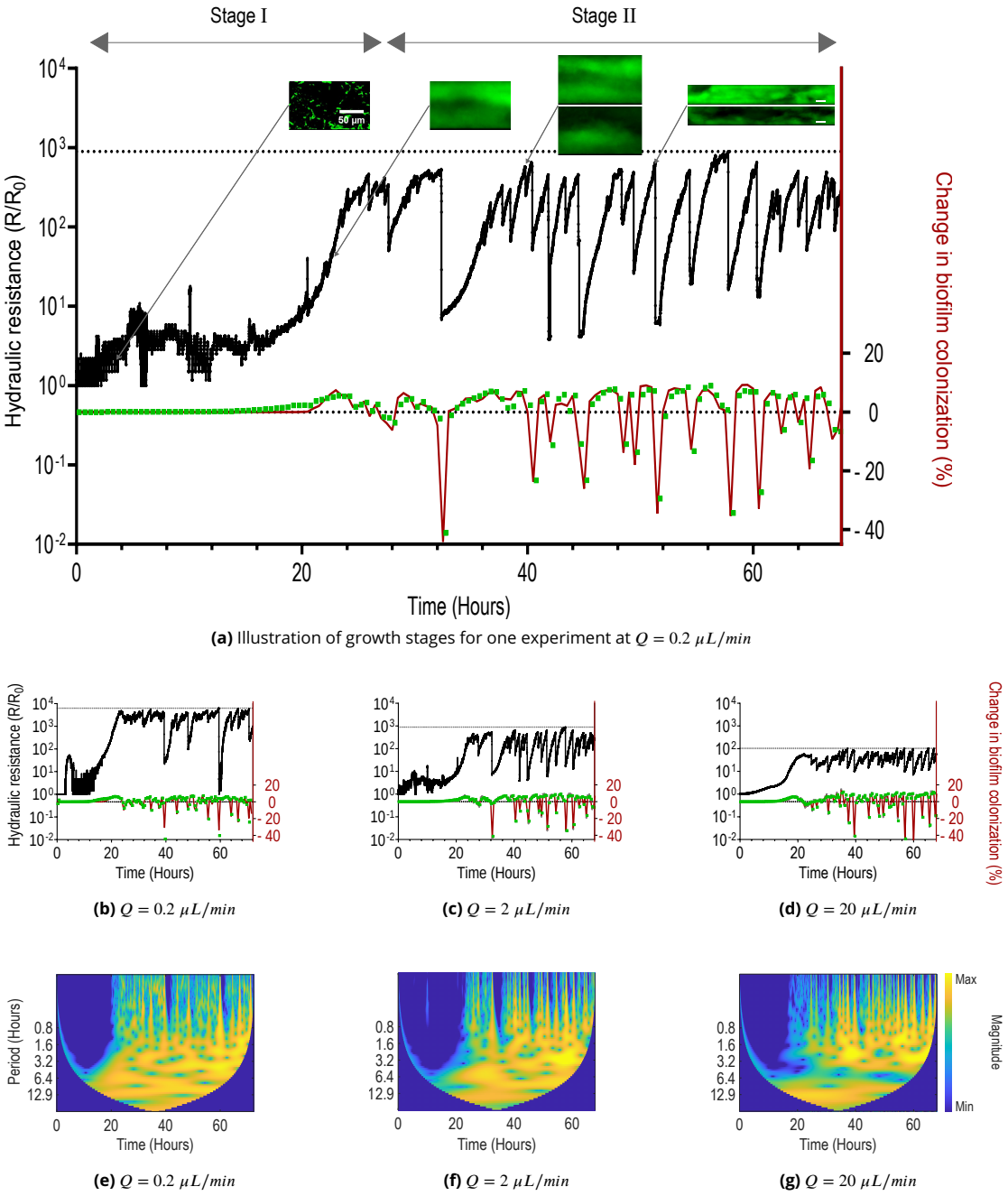


**(a)** Illustration of growth stages for one experiment at $Q = 0.2\ \mu L/min$

**(b)** $Q = 0.2\ \mu L/min$ **(c)** $Q = 2\ \mu L/min$ **(d)** $Q = 20\ \mu L/min$

**(e)** $Q = 0.2\ \mu L/min$ **(f)** $Q = 2\ \mu L/min$ **(g)** $Q = 20\ \mu L/min$

**Figure 3.** Temporal dynamics of growth and detachment for $Q = 0.2\ \mu L/min$, $2\ \mu L/min$ and $20\ \mu L/min$. (a): Summary of the two main stages of biofilm development. The figure shows the evolution of the hydraulic resistance (black solid line) in time, calculated from pressure measurements, and microscopy images corresponding to the different phases. It also shows changes in biofilm colonization extracted from either integrated fluorescence intensity (green squares) or from image segmentation (red solid line). (b), (c) and (d): Temporal dynamics of growth and detachment for the different flow rates. (e), (f) and (g): Wavelet scalograms corresponding to (b), (c) and (d).

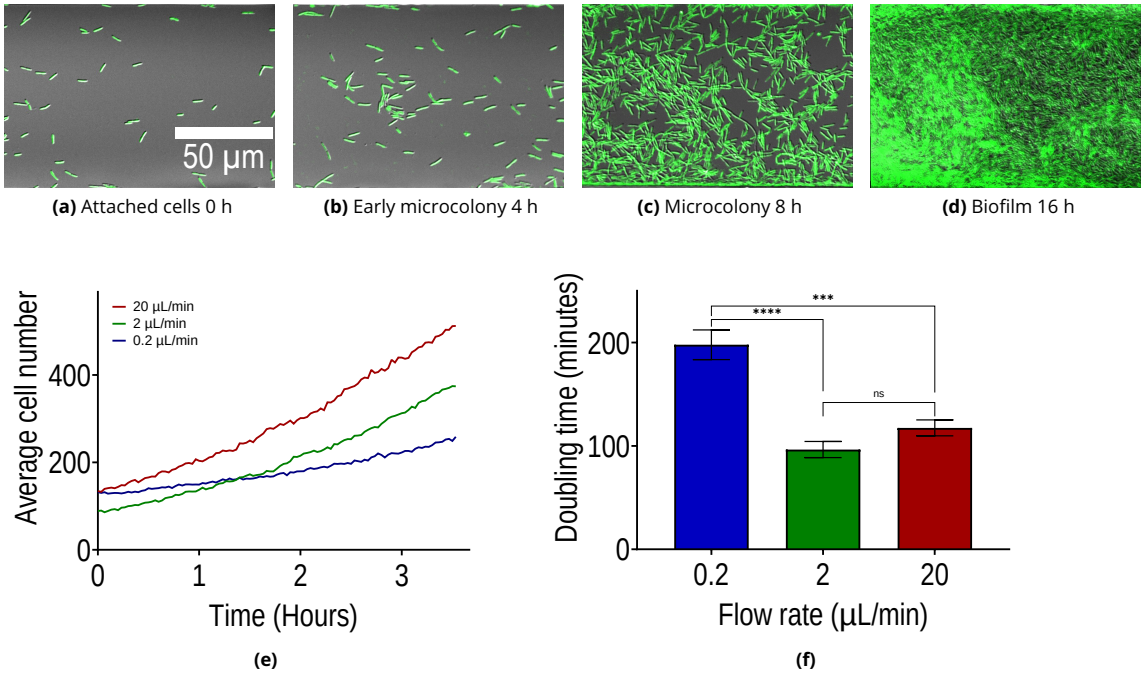


**Figure 4.** Flow modifies the apparent doubling time of bacteria on surfaces. (a), (b), (c) and (d): Composite brightfield and GFP images of development stages, starting from single cells that form microcolonies and then evolve towards a biofilm. (e) and (f) show, respectively, the average number of cells on the surface as a function of time and the corresponding doubling time for flow rates ($Q = 0.2\ \mu L/min$, $2\ \mu L/min$ and $20\ \mu L/min$). For (f), statistical differences were examined by unpaired student test with Gaussian distribution of data and equal standard deviations. Error bars indicate standard error of mean (SEM) and symbols denote statistical significance (****: p-value <0.0001, ***: p-value = 0.0002, ns: p-value > 0.05). The doubling time was calculated by a linear fitting of the logarithm of the number of cells. The slope was used to estimate growth rate and doubling time. Cell count was calculated from image segmentation of four positions in two channels to generate 8 measurements by condition (n= 8) for ($Q = 0.2\ \mu L/min$, $2\ \mu L/min$ and $20\ \mu L/min$).

stages in the colonization of the channel. Combined with a model for the distribution of biofilm in the cross-section of the channel – we treated the biofilm as a uniform layer – it was used to indirectly evaluate a mean volume fraction of biofilm, $\phi$. We further visualized directly the channel using timelapse microscopy with differential interference contrast, bright field and fluorescence imaging.

We found that biofilm development occurs in different phases, in a way that is consistent across flow rates. We propose to decompose the dynamics in two main components: Stage I that corresponds to the initial adhesion, growth and saturation; and stage II that features large fluctuations in the amount of biomass in the channel. Fig 3(a) illustrates our decomposition in two stages on the temporal evolution of $\frac{\mathcal{R}}{\mathcal{R}_0}$ in the case $Q = 0.2\ \mu L/min$. The following details the dynamics of Stages I and II.

## Early stage I is driven by surface adhesion, motility, division and colony formation

Our inoculation process results in the sparse attachment of individual bacterial cells on the boundaries of the channel. On the glass slide, we evaluated the initial density to be about 38800 cells per $mm^2$. Growth of adhered cells started straight away upon flowing the culture medium, with little to no lag time. The apparent macroscopic lag, as visible in Fig 3, does not stem from a lag at the cellular level, but rather from the sensitivity of the pressure measurements. The relative hydraulic resistance, $\frac{\mathcal{R}}{\mathcal{R}_0} = \frac{1}{(1-\phi)^2}$, can be linearized as $\frac{\mathcal{R}}{\mathcal{R}_0} \sim 1 + 2\phi$ when $\phi \ll 1$. The evolution of $\frac{\mathcal{R}}{\mathcal{R}_0}$ with $\phi$ is thus affine at the beginning of the experiment, with small changes in the hydraulic conductivity that could not be detected in our experimental system. This generates some amount of noise in the early signal, that tends to decrease when increasing flow rate.

To characterize the growth time at the cellular level, we calculated an apparent doubling time at the cellular level from microscopy images of cells attached to the glass slide in the very early stage (from 0 to 3.5 hours, see Fig 4). We first segmented images from differential interference contrast microscopy to identify individual bacteria on the surface and then fitted linearly the log of the number of cells as a function of time. Calculated doubling times were measured as about 198, 95 and 117 minutes on average for, respectively, $Q = 0.2\ \mu L/min$, $2\ \mu L/min$ and $20\ \mu L/min$. As a reference, the doubling time in liquid culture was measured as about 110 minutes (standard deviation of $\sim$ 10 minutes). Although understanding exactly what generates this dependence of the doubling time upon the flow rate is beyond the scope of this paper, it is worth noting that nutrient limitation is not likely to play a role, as we have previously validated the fact that there is no limitation for $Q \geq 0.2\ \mu L/min$, even when biofilm has formed. Mechano- and rheo-sensing could be involved, with bacteria directly regulating their response to perceived shear stress or rate (***Sanfilippo et al., 2019***; ***Rodesney et al., 2017***), as well as heterogeneities in the rate of division – for instance between motile and adhered cells (***Rossy et al., 2019***) – or in the attachment/detachment dynamics.

After this initial phase, colonies expand and produce large quantities of EPS that yield a much sharper increase of the hydraulic resistance. This increase is linked to a combination between the exponential growth of the microorganisms and the production of the EPS, but also to the nonlinear relationship between $\frac{\mathcal{R}}{\mathcal{R}_0}$ and $\phi$, $\frac{\mathcal{R}}{\mathcal{R}_0} = \frac{1}{(1-\phi)^2}$.

### Late Stage I reflects an equilibrium between growth and detachment

We observe an inflection of the signal in late Stage I in Fig 3. This inflection corresponds to the end of the rapid growth phase, with flow-induced detachment progressively increasing, until detachment equilibrates with growth. To further understand this effect, let us consider the mass balance of biofilm in the zone of interest in the channel. The inlet flux of bacteria is zero, since our UVC system prevents growth outside the zone of interest. The source of biomass therefore only results from the uptake of nutrients, division of bacterial cells and EPS production. The sink of biomass is due to flow-induced removal, which includes parts of the biofilm that are displaced out of the zone of interest through the flow/remodelling of the biofilm at the outlet, and parts that are washed away by erosion and seeding (***Kaplan, 2010***; ***Krsmanovic et al., 2021***). In the absence of nutrient limitation, we can estimate the evolution of the biovolume in the channel from the ordinary differential equation

$$\dot{\phi} = \phi \left(1 - \frac{1-\phi_{\max}}{1-\phi}\right), \tag{5}$$

which is a direct simplification of Eq 3 with $\phi$ describing an average volume fraction in the entire channel, and thus being only a function of time. This model captures a competition between growth and different types of smooth detachment (flow, seeding, erosion).

### Stage II features sloughing-induced jump events followed by re-growth

After growth and detachment start to equilibrate at the end of Stage I, sloughing events become particularly important. These are visible in Fig 3 as jumps in the hydraulic resistance (see also the blue stripes on the wavelet scalograms in Fig 3), which correlate with sharp changes in the biofilm colonization of the channel. The jumps correspond to a range of different events, from minor detachment – where a relatively small portion of the biomass is detached – to major sloughing – where a large portion of the biomass is detached. Fig 5 shows example microscopy images of such events.

To better visualize the spatio-temporal dynamics and connect the different observations for the pressure and microscopy, we plotted kymographs in Fig 5 (see also SI figures S7, S10 and S13), showing both variations in time and in space, along with the corresponding hydraulic resistance signal. These graphics show clearly the correlation between the pressure signal on the right-hand side and the detachment events on the kymographs. We can readily identify that large drops in

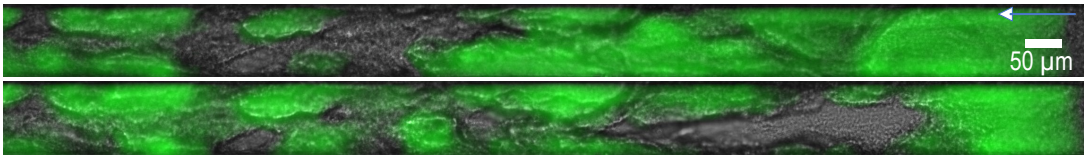


**(a)** Minor event

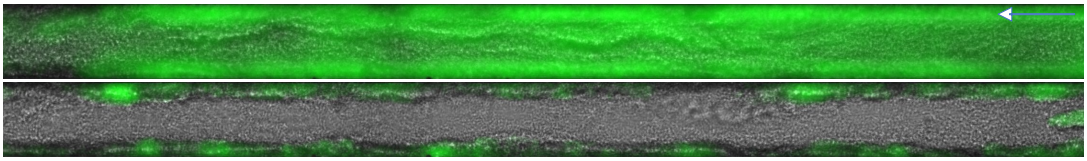

**(b)** Major event

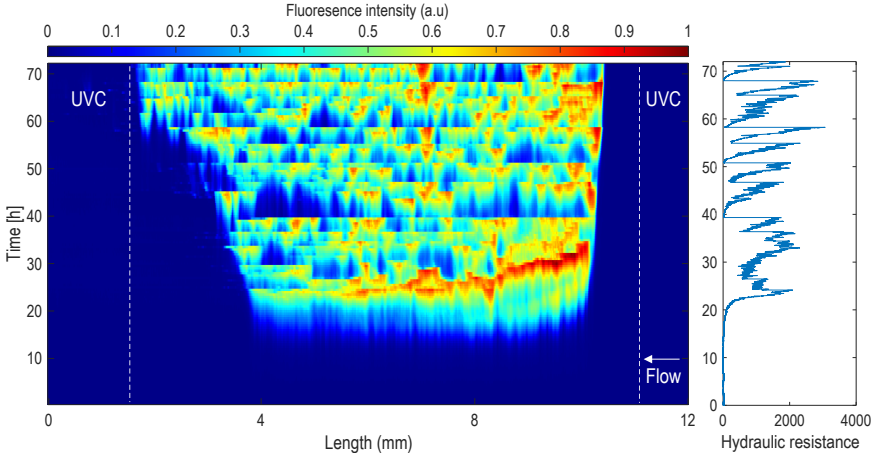


**(c)** $Q = 0.2\ \mu L/min$

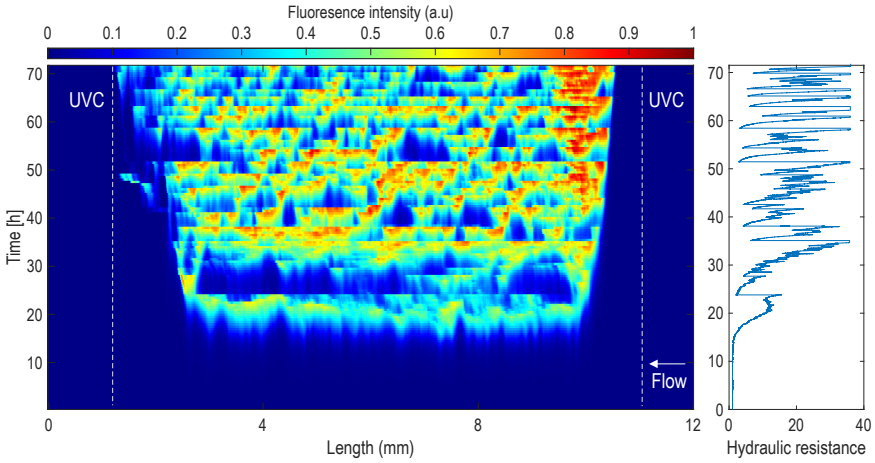


**(d)** $Q = 20\ \mu L/min$

**Figure 5.** Spatio-temporal dynamics of sloughing in Stage II. (a) and (b): composite bright field and GFP image of a 40 hour biofilm during Stage II. Image before (top) and after (bottom) for (a) a minor sloughing event and (b) a major sloughing event. (c) and (d): kymographs showing the fluorescence intensity (averaged in the radial direction $y$) as a function of both the longitudinal direction ($x$) and time. Fluorescence intensity values were normalized by the maximum value. Plots on the right-hand side show the corresponding hydraulic resistance as a function of time.

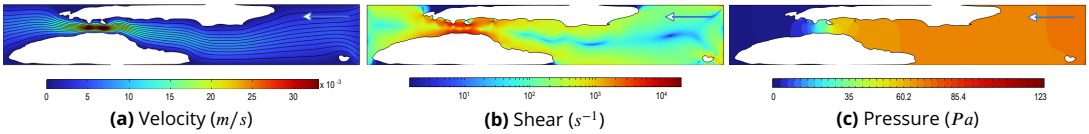


**(a)** Velocity ($m/s$) **(b)** Shear ($s^{-1}$) **(c)** Pressure ($Pa$)

**Figure 6.** 2D simulations of flow around a biofilm (white) in a channel of $100\,\mu m$ width and $500\,\mu m$ length using COMSOL multiphysics. (a): Streamlines and magnitude of the velocity ($m/s$). (b): Shear rate in ($s^{-1}$). (c): Pressure field in ($Pa$). The white arrows indicate the flow direction.

pressure correspond to large events with detachment over almost the entire length of the microchannel. We also visualize a range of detachment events corresponding to various sizes of biofilm being detached, along the rapid increase of resistance and biomass following each sloughing event.

Each sloughing event is followed by a rapid growth phase resembling late Stage I, leading to a cycle of successive sloughing and re-growth. In each re-growth phase, we observe a sigmoid-like shape of the hydraulic resistance signal that is similar to Stage I. As in Stage I, the maximum stems from an equilibrium between growth and detachment. $\phi_{\text{max}}$ thus corresponds to a critical value of the stress, $\sigma_{\text{crit}}$, that generates enough detachment to compensate growth. From Eqs 2-3, this reads

$$\sigma_{\text{crit}} = \sigma_0 \frac{\mathcal{R}_{\text{max}}}{\mathcal{R}_0}, \tag{6}$$

with $\mathcal{R}_{\text{max}}$ the maximum value of the hydraulic resistance. The maximum value of the hydraulic resistance over all stages of development decreases by orders of magnitudes from $0.2$ to $20\,\mu L/min$ – $\frac{\mathcal{R}_{\text{max}}}{\mathcal{R}_0} \simeq 8.2 \times 10^3$ for $0.2$, $\simeq 8.4 \times 10^2$ for $2$ and $\simeq 1.0 \times 10^2$ for $20$. We can thus estimate the critical stress at about $\sigma_{\text{crit}} \simeq 100 - 200\,Pa$.

### Pressure becomes prominent in late Stage I and Stage II

Here, we ask the question of the nature of the hydrodynamic stress and, in particular, whether the hydrodynamic stress is dominated by shear or pressure. We are particularly interested in understand the nature of $\sigma_{\text{crit}}$. Fig 6 shows simple 2D flow simulations illustrating the types of stress induced by the flow of a viscous fluid upon the biofilm. We see that the shear stress becomes particularly strong in the bottlenecks and that the pressure difference also builds up, therefore generating both shear and pressure stresses. In the initial stages of bacterial development, when only individual cells and microcolonies are adhered to surfaces, we expect the dominant stress to be shear. However, what happens in later stages for large fractions of biofilm?

A simple approach to quantifying the relative importance of stresses in our system is to consider the case of uniform film growth between the UVC zones (see details in supplementary information). The tangential stress at the solid/biofilm surface is $\frac{\sigma}{\sigma_0} = (1-\phi)^{-2}$, with a contribution from shear $\frac{\sigma_{\text{shear}}}{\sigma_0} = (1-\phi)^{-1}$ and from pressure $\frac{\sigma_{\text{pressure}}}{\sigma_0} = \phi\,(1-\phi)^{-2}$. In the case of a fixed flow rate, we therefore have $\frac{\sigma_{\text{shear}}}{\sigma_0} \to 1$ and $\frac{\sigma_{\text{pressure}}}{\sigma_0} \to 0$ in the limit $\phi \to 0$; $\sigma_{\text{shear}} = \sigma_{\text{pressure}}$ for $\phi = 0.5$; and $\sigma_{\text{pressure}} > \sigma_{\text{shear}}$ for $\phi > 0.5$. This simple conceptualization confirms that pressure stress tends to become dominant when a large portion of the channel is colonized in late late Stage I and in Stage II.

### Maximum clogging depends on the flow rate and the matrix composition

In our experiments, the maximum values of the volume fraction, estimated from hydraulic resistance, are $\phi_{\text{max}}\,(Q = 0.2) = 0.989$ for $0.2$, $\phi_{\text{max}}\,(Q = 2) = 0.966$ for $2$ and $\phi_{\text{max}}\,(Q = 20) = 0.901$ for $20$ (see Fig 7 and Table 1) – remarkably, this maximum is very reproducible across replicates, with standard deviations for volume fractions in the range of $10^{-3}$ in our experiments (Fig 7).

The model Eq 5 for Stage I is consistent with this dependence upon the flow rate. By definition of $\phi_{\text{max}}$ in Eqs 2-3 and in Eq 5, we have

$$\phi_{\text{max}} = 1 - \frac{\chi X}{Y\alpha\,(1+K^\star)} \left(\frac{A}{4}\frac{\mu Q}{h^3}\right)^{\frac{1}{2}}. \tag{7}$$

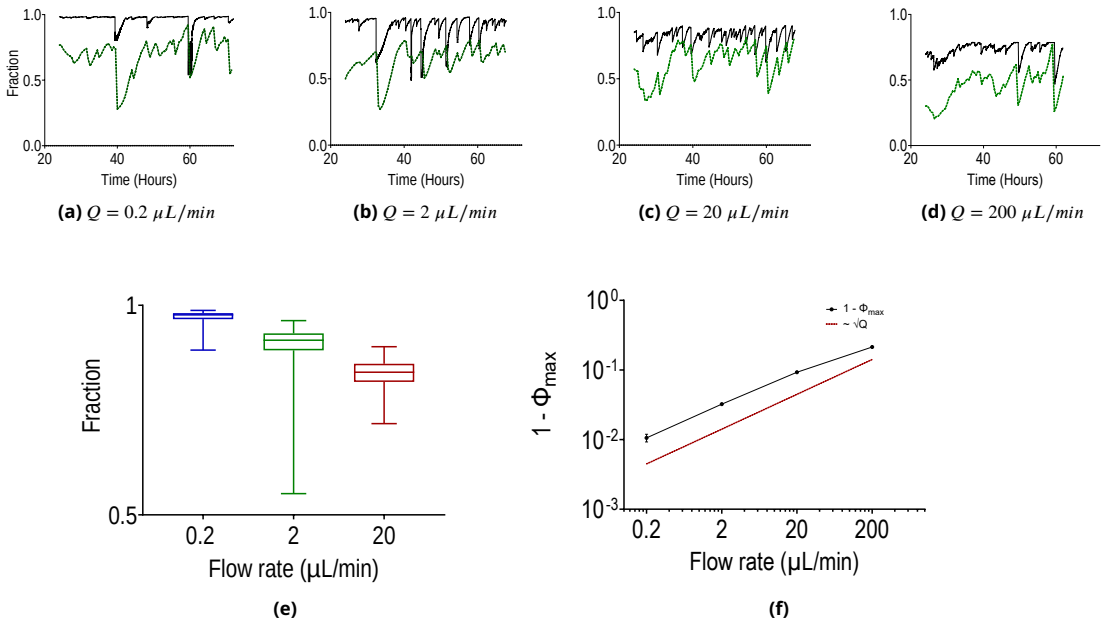


**Figure 7.** Evolution of the distribution and maximum of the volume fraction for the different flow rates. (a), (b), (c) and (d): Fractions of biofilm in the microchannel, either calculated from hydraulic resistance (black solid line) or estimated from integrated GFP intensity (green dotted line), for the different flow rates. (e): Distribution of biofilm fraction between 24 and 72 h for all flow rates, represented as whisker boxes. (f): Log-log plot of $1 - \phi_{\max}$ as a function of the flow rate ($Q = 0.2\ \mu L/min$, $2\ \mu L/min$, $20\ \mu L/min$ and $200\ \mu L/min$). The red dotted line simply shows the slope for an evolution with the square root of the flow rate.

We can express this relatively to a reference flow rate as

$$\frac{1-\phi_{\max}(Q)}{1-\phi_{\max}(Q_{\text{ref}})} \propto \left(\frac{Q}{Q_{\text{ref}}}\right)^{\frac{1}{2}}. \tag{8}$$

Upon considering $Q_{\text{ref}} \equiv 0.2$ with $\phi_{\max}(Q_{\text{ref}}) = 0.989$, we obtain $\phi_{\max}^{\text{theoretical}}(Q = 2) \simeq 0.966$ and $\phi_{\max}^{\text{theoretical}}(Q = 20) \simeq 0.901$ from Eq 8. These values are in excellent agreement with the experiments (see Table 1).

To further validate this idea that $\phi_{\max}$ decreases with the square root of the flow rate, we performed a single experiment at $200\ \mu L/min$. Results in Fig 7 indicate that the behavior is similar to that of other flow rates, but with a significantly lower value of $\phi_{\max} \simeq 0.786$. We also see that the scaling remains remarkably similar with $1 - \phi_{\max} \sim Q^{\frac{1}{2}}$ in the range $[0.2,\ 200]$ – equivalently, the scaling for the hydraulic resistance is $\mathcal{R}_{\max} \sim Q^{-1}$ (see Fig S18). The fact that the model can recover the correct scalings is an important validation of our modeling hypotheses, in particular that the detachment rate depends on square root of the hydrodynamic stress.

Modifications of the composition and mechanical properties of the biofilm, in particular if they affect $\chi$ or sloughing, should have a significant impact on the value of $\phi_{\max}$. Among *P. aeruginosa* PAO1 polysaccharides – Pel, Psl and alginate – Pel and Psl are considered the two primary components of the EPS matrix structure (***Ryder et al., 2007***), controlling the cohesive and adhesive strength of the biofilm. We therefore performed experiments with mutants that cannot produce either Pel or Psl, with the idea that this should modify the value of $\chi$. The Psl mutant is a *pslD* deficient $\Delta psl\,D$ obtained from *P. aeruginosa* PAO1 by non-polar allelic exchange (***Colvin et al., 2012***). The Pel mutant is a pelF deficient strain $\Delta pel\,F$ also obtained by allelic exchange (***Colvin et al., 2011***). Liquid culture showed that the lag and doubling times were, respectively, 233.36 and 105.5 minutes (see Fig S21). Fig 8 (see also S14, S15, S16 and S17) shows the behavior of mutants compared to the wild type. We found that the volume fraction of biofilm was significantly lower for both mu-

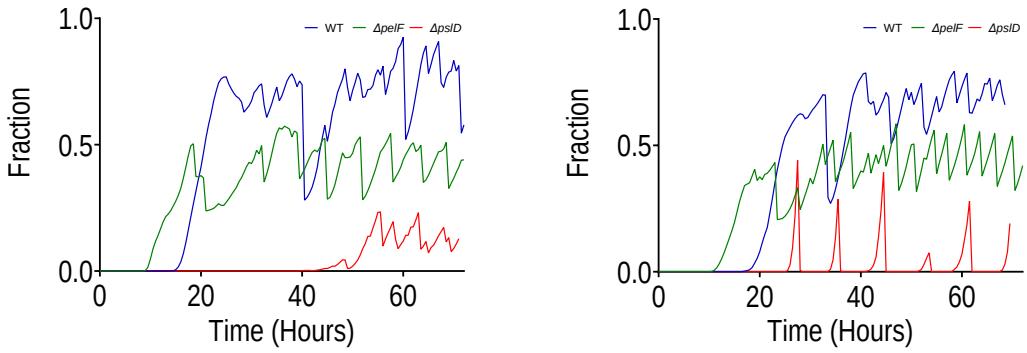


**(a)** $Q = 0.2\ \mu L/min$ **(b)** $Q = 2\ \mu L/min$

**Figure 8.** Fraction of biofilm obtained from image segmentation for the Δ*psl* (red line) and Δ*pel* strains (green line) compared to the wild-type strain (blue line), for ($Q = 0.2\ \mu L/min$, $2\ \mu L/min$).

tants and that the Psl mutant was more strongly affected than the Pel mutant. The Psl mutant only weakly attached to the surface and was more prone to detachment – an observation that is consistent with the prominent role of Psl in the mechanics of PAO1 biofilms (***Colvin et al., 2011***). For the case $2\ \mu L/min$, we even observed an almost complete detachment of the biofilm with only few cells remaining attached and making re-growth possible after a sloughing event. At $20\ \mu L/min$, we could not detect the presence of biofilm.

## Sloughing can be understood as a stochastic process

The model presented so far can describe Stage I and the signal in between two sloughing events, but not the catastrophic jumps associated with sloughing. To characterize the latter, we first performed a frequency analysis of the signal, as shown in Fig 9a. This approach did not prove very informative as it essentially shows a power spectrum typical of noise, with a slope roughly smaller than -2. This result, however, motivated the construction of a more physical representation of the process. The basis of this representation is the observation that fluctuations have a very specific signature on the hydraulic resistance: they first feature a sharp decrease due to sudden sloughing, followed by a slower increase due to growth. Since growth and smooth biofilm detachment are already described in the model, this observation suggests that we only need to capture the sudden sloughing to improve the description. The model takes the form of the following stochastic differential equation,

$$d\phi_t = \phi_t \left(1 - \frac{1-\phi_{\max}}{1-\phi_t}\right) dt - \phi_{t^-} dN_t, \tag{9}$$

with $\phi_t$ describing the average fraction of biofilm in the microchannel, $N$ the jumps and $\phi_{t^-}$ the value of $\phi$ at time $t^-$ just before the jump.

The challenging part of this representation is to accurately describe the randomness of the process $N$ – which is likely strongly dependent upon spatial heterogeneities, for instance in the initial attachment of bacteria. We characterized $N$ in our experiments via the distributions of both the times between two successive jumps and the relative amplitudes of the jumps – i.e. the amplitude of each jump divided by the value of the volume fraction just before the jump $\phi_{t^-}$. Fig 9 shows histograms of these distributions extracted from signal processing of the experimental data (see Material and Methods). We see that the distribution of times between successive jumps, $\delta t$, can be well approximated by a Gamma distribution – solid lines in Fig 9 for a fit of the experimental data. The relative amplitude of each jump $\xi = {}^{\Delta\phi}/_{\phi_{t^-}}$ was better represented by log-normal distributions – solid lines in Fig 9 for a fit of the experimental data. Example realizations of the simulations are presented in Fig 9 for the flow rates used in the experiments. Simulations are strikingly similar to experimental data, thus suggesting that sloughing can indeed be accurately modeled as a

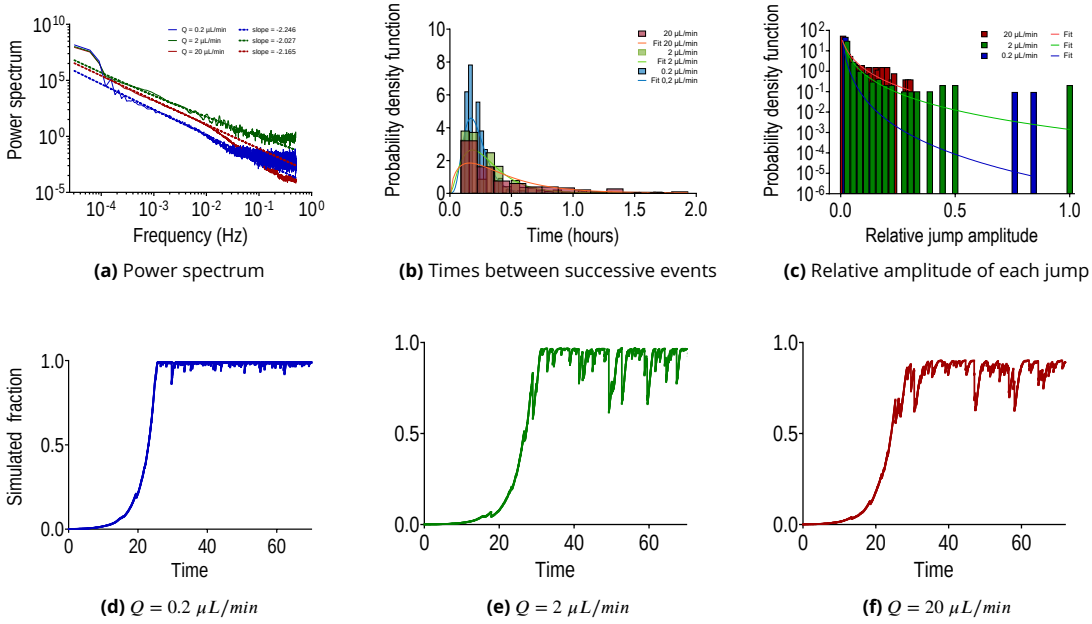


**(a)** Power spectrum **(b)** Times between successive events **(c)** Relative amplitude of each jump

**(d)** $Q = 0.2\ \mu L/min$ **(e)** $Q = 2\ \mu L/min$ **(f)** $Q = 20\ \mu L/min$

**Figure 9.** Stage II detachment events can be described as a jump process. (a) Power spectrum for the different flow rates ($Q = 0.2\ \mu L/min$, $2\ \mu L/min$ and $20\ \mu L/min$). Slopes are indicative and were calculated in the interval between 0 and 0.25 Hz. (b) Probability density function of the time between two successive jump events, $\delta t$, for ($Q = 0.2\ \mu L/min$, $2\ \mu L/min$ and $20\ \mu L/min$). The histograms are calculated from experiments, while the solid lines are fitted Gamma distributions ${(\delta t)^{a-1}}/{(b^a \Gamma(a))} \exp(-\delta t/b)$. (c) Probability density function of the relative amplitude of jump events, $\xi = {\Delta\phi}/{\phi_{t-}}$, for ($Q = 0.2\ \mu L/min$, $2\ \mu L/min$ and $20\ \mu L/min$). The histograms are calculated from experiments, while the solid lines are fitted log-normal distributions ${1}/{\left(\xi\sigma\sqrt{2\pi}\right)} \exp\left(-{(\ln\xi-\mu)^2}/{(2\sigma^2)}\right)$. (d), (e) and (f): Stochastic simulations of the volume fraction as a function of time for ($Q = 0.2\ \mu L/min$, $2\ \mu L/min$ and $20\ \mu L/min$).

stochastic jump process.

## Discussion

### Regimes of nutrients and oxygen transport

Our experimental setup, which implements a novel UVC strategy to confine biofilm development within a specific zone in the channels, allowed us to finely control boundary conditions and study the role of molecular transport on biofilm development. Our results suggest that, in confined channels, the longitudinal distribution of biofilm ensues from a competition between advective transport of solutes along the channel and uptake by the cells. Modeling molecular transport as an advection-diffusion-reaction equation, this effect can be quantified using the ratio of longitudinal Péclet and Damköhler numbers, $Pe/Da$, which compares advection to reaction. When $Pe/Da < 1$, biofilm growth is nutrient-limited and localized close to the inlet. When $Pe/Da > 1$, biofilm development is close to homogeneous. In the radial direction, the limitation can be characterized in a similar way via a radial Damköhler number, $Da_{\text{radial}}$, defined as the ratio of reaction and radial diffusion. In our experiments, we always had $Da_{\text{radial}} < 1$ with only weak gradients and no radial limitation.

Although the competition between advective/diffusive transport and uptake is a universal feature of biofilm development in flow, the solute that becomes limiting depends on the details of the setup. In our experiments, we found that nutrients were restricting growth, while other works in microchannel flows, such as (***Thomen et al., 2017***), found that the effect of oxygen was dominant. Several factors play an important role here, including the composition of the growth medium, the catabolism of the microorganisms, the kinetics or even the resilience of bacteria to low oxygen concentration. For instance, ***Thomen et al.*** (***2017***) focused on an *E. coli* K12 derivative. *E. coli* can respond strongly to micro-aerobiosis (***Colón-González et al., 2004***), whereas *P. aeruginosa* is known to be more resilient (***Sabra et al., 2002***; ***Alvarez-Ortega and Harwood, 2007***). Factors that affect transport characteristic times, such as the flow velocity or the dimensions of the channels, also modify the competition with uptake. The length of the channel modulates the time for advective transport along the channel and therefore the ratio $Pe/Da$. The width and height control the characteristic time for radial diffusion. In ***Thomen et al.*** (***2017***), for instance, the width of the channel is $1000\ \mu m$ so that diffusion takes about 100 times longer and $Da_{\text{radial}}$ is 100 times larger than for $100\ \mu m$ channels.

### Temporal dynamics and hydrodynamic stresses

With these regimes clearly identified for molecular transport, we could then study the effect of hydrodynamic stresses on biofilm development and, in particular, the role of flow-induced detachment on the spatio-temporal dynamics. We suppressed any form of nutrient limitation, either radial or longitudinal, by focusing on flow rates $\geq 0.2\ \mu L/min$ with $Pe/Da > 1$ and $Da_{\text{radial}} < 1$. In so doing, we found that the time response featured two distinct stages: the hydraulic resistance first followed a relatively standard sigmoid-like pattern (Stage I), but then switched to a different regime with large self-sustained fluctuations (Stage II). As discussed in what follows, we argue that this Stage II is a signature effect of biofilm development in confined flow.

Stage I began just after initial inoculation, as soon as the culture medium started flowing in the microchannel. Early Stage I was dominated by cell adhesion, division, surface motility and microcolony formation. The average velocity in the channel at $0.2\ \mu L/min$ is above $300\ \mu m/s$ so bulk motility is likely not playing an important role when $Q \geq 0.2\ \mu L/min$ (***Rossy et al., 2019***). Contrary to ***Thomen et al.*** (***2017***) – where no direct initiation of the biofilm of *E. coli* biofilm was possible above a shear stress of $10\ mPa$ – our results show that *P. aeruginosa* PAO1 strongly adhered to the surface and could initiate biofilm formation for all shear stresses. We even observed that the apparent doubling time within the first few hours of growth was the smallest in the case at $2\ Pa$. Stage I then evolved towards the standard steps of biofilm formation for *P. aeruginosa* (***Rasamiravaka***

*et al., 2015*; *Krsmanovic et al., 2021*), with clonal microcolonies that extended, joined together and grew into mature biofilms. The exponential growth and EPS production yielded a sharp increase of the hydraulic resistance by several orders of magnitude, which is consistent with previous works (*Cunningham et al., 1991*; *Desmond et al., 2022*).

Stage II was characterized by large fluctuations in the hydraulic resistance and in the quantity of biomass in the channel. We showed that these fluctuations are the result of successive cycles of growth and sloughing events: parts of the biofilm get detached by the flow upon reaching a critical stress, generating sharp discrete-like events of detachment, followed by a fast re-growth of the biofilm. In both late Stage I and in Stage II, pressure-induced stresses play a crucial role. Most works have focused on shear stress (*Krsmanovic et al., 2021*; *Kurz et al., 2022*; *Telgmann et al., 2004*; *Wagner et al., 2010*; *Paul et al., 2012*) because, in many situations, such as biofilm development in large reactors, the effect of pressure can be neglected. However, this is not the case in confined systems, where biofilm can clog a large proportion of the flow channels and the pressure build-up induced by clogging can generate an important force on the biofilm.

## Maximum clogging

One aspect that stands out in our experiments, because of its physical meaning and reproducibility across replicates, is the concept of maximum clogging. In Stage I and after each sloughing in Stage II, curves for the hydraulic resistance had a sigmoid-like shape, with an inflection that was a signature of a competition between growth and smooth detachment due to erosion, seeding and biofilm flow outside the zone of interest. We found that the maximum value of the hydraulic resistance across the entire experiment scales with the inverse of the flow rate, which is consistent with the modeling hypothesis that smooth detachment scales with the square root of the hydrodynamic stress (*Rittman, 1982*; *Duddu et al., 2009*; *Coyte et al., 2017*). This concept of maximum clogging can also be expressed as a critical value of the hydrodynamic stress generating enough detachment to compensate growth. In our framework, this equilibrium stress was in the order of 100-200 Pascals for the wild type and did not vary significantly with the flow rate.

To further understand the role of the EPS matrix composition on maximum clogging, we studied the behavior of Δpsl and Δpel mutants. Pel and Psl are the two main exopolysacharides produced by nonmucoid strains of *P. aeruginosa*. For both mutants, the maximum amount of biofilm in the microchannel was lower than for the wild type, thus indicating that these mutants were more easily detached by the flow. We also found that Psl had a stronger impact than Pel on the spatio-temporal dynamics and, in particular, on maximum clogging. The Δpsl mutant featured major sloughing events for $2\ \mu L/min$ that led to a near-complete removal of the biofilm. For $20\ \mu L/min$, we observed a complete removal. On the other hand, Pel featured a dynamics similar to that of the wild type, but with a reduced maximum clogging.

Although critical stresses are widely used in characterizing flow-induced detachment of biofilms, they have a broad range of different meanings and values. Critical stresses have been used to characterize a form of complete detachment from the solid surface (*Jiang et al., 2021*). *Ohashi and Harada* (*1996*) described an adhesion strength as the stress required to remove the biofilm – upon conceptualizing the problem as a surface to surface bonding, the adhesive strength has also be defined as the work required to detach the biofilm from the surface per surface area (in Joule per $m^2$) (*Chen et al., 1998*). *Ohashi and Harada* (*1996*) found values for the shear strength in the hundreds of Pascals. *Lau et al.* (*2009*) measured an adhesive pressure – adhesive force measured by microbead force spectroscopy divided by contact area – for *P. aeruginosa* PAO1 that was in the tens of Pascals. *Körstgens et al.* (*2001*) studied the yield strength of a mucoid *P. aeruginosa* strain, discussing its role in the mechanical failure of the biofilm. Considering the biofilm as a viscoelastic gel with plastic flow properties, they found a stress at failure close to $1000\ Pa$. *Lee et al.* (*2023*) show that bio-aggregates of *E. coli* at pore throats become fluidized above a critical value of the shear stress with a yield point at roughly $1.8\ Pa$.

To establish a clear link between these values, our critical stress at 100-200 Pascals and the

observed dynamics of sloughing in Stage II, future works will need to further refine our understanding of the role of the different variables on flow-induced detachment, including distributions of stresses within biofilms, adhesive strength to surfaces, mechanical properties of the biofilm, and biological regulation through e.g. quorum sensing (***Emerenini et al., 21 juil. 2015***) and/or rhamnolipids production (***Boles et al., 2005***).

### Self-sustained fluctuations

Large fluctuations of the hydraulic resistance, similar to that observed in our Stage II, were previously reported in a few works on porous media flows. ***Howell and Atkinson*** (***1976***) showed that, in trickling filters, constant influent concentration and operating conditions can yield large fluctuations induced by sloughing events. ***Stewart and Scott Fogler*** (***2002***) found very large oscillations in the pressure signal due to the formation of successive stable or unstable dextran plugs of *Leuconostoc mesenteroides* biofilm, behaving in a way similar to a yield stress fluid, and allowing flow only through breakthrough channels – see also discussions on the flow of yield stress fluids through porous media in (***Talon, 2022***). ***Sharp et al.*** (***2005***) showed that "the pore channels are dynamic, changing in sized, number and location with time" in a flat plate reactor colonized by *Vibrio fischeri* biofilm. ***Kurz et al.*** (***2022***) found successive cycles of growth and shear-induced detachment in the preferential flow paths for *Bacillus subtilis* biofilm development in a microfluidic system with cylindrical obstacles. ***Bottero et al.*** (***2013***) modeled the coupled effects of flow, clogging and detachment to study the mechanisms that control these self-sustained fluctuations, in particular what leads to the clogging of a preferential flow path and the unclogging of another one – contrary to the development of stable flow paths.

Although there are similarities with our observations, porous media have an inherent degree of complexity in the geometry that, combined with the nonlinear response of biofilms, can lead to a range of complex mechanisms. For instance, some of the works above-mentioned identified changes in the flow paths associated with the fluctuations. Our work shows that, even in a single channel with continuous flow, these fluctuations occur and prevent the system from reaching a true steady-state. This observations leads us to propose that the self-sustained fluctuations observed in Stage II are a signature of biofilm development in confined flows and may occur in the simplest geometries. The underlying idea is that the strong bioclogging in confined geometries generates a pressure build-up that is the main cause of sloughing. Once a large part of the biofilm gets detached, the pressure decreases and the biofilm can re-grow to get a new cycle started. Our work therefore highlights the ubiquity of these fluctuations, which are likely to play a key role in the development and spreading of biofilms in a range of different systems, such as clogging in pipes, catheters (***Stickler, 2014***) or stents (***Guaglianone et al., 2010***), with applications ranging from infections, to environmental processes and engineering systems.

### Stochastic modeling

Our approach to modeling was constructed in two main parts. We first proposed differential equations to describe nutrient transport coupled with the dynamics of biofilm development in the channel, including growth and smooth detachment. The sharp jumps corresponding to sloughing were then added to this first layer of the model as a jump stochastic process. Although it seems quite natural to characterize the statistics of detachment (***Wilson et al., 2004***), there are actually very few attempts to treat such problems in the framework of stochastic processes. ***Howell and Atkinson*** (***1976***) modeled sloughing in trickling filters through a conceptualization as connected filter units describing the discrete pieces of packing material in the filter. They introduced randomness by permitting sloughing at multiples of a fixed time interval. ***Bohn et al.*** (***2007***) used an approach combining a logistic growth with random sloughing events through a stochastic differential equation. They described sloughing via a discrete expression of the amplitude of jumps occurring independently at each time step, which allowed them do describe daily fluctuations in light absorbance data for phototrophic biofilms development in a flow-lane incubator. In our approach, the jump process

was characterized by two random variables: the interevent time between two successive jumps and the relative amplitudes of the jumps. Through the analysis of experimental data, we reconstructed the probability density functions for these random variables, with respectively Gamma and log-normal distributions.

There have been previous discussions (***Lewandowski et al., 2004***) on the determinism of biofilm formation, suggesting that sloughing events are intrinsically random events that generate large fluctuations, prevent the system from reaching a steady state and hinder the reproducibility of long-term experiments. Our work confirms that sloughing is integral to biofilm development (***Telgmann et al., 2004***) in confined flows but shows that, although a true steady state is never reached, the fluctuations can be precisely characterized using stochastic modeling. This approach paves a way forward in terms of reproducibility: even though the state of the biofilm at any given time may not be reproducible, the randomness of the process may very well be.

Our approach to characterizing bursting events in terms of the distribution of the amplitude and interevent time is reminiscent of the description of other physical systems, such as avalanches (***Maaß et al., 2015***). For earthquakes, for example, a Gamma distribution for interevent times has been found in many different geographic regions (***Corral, 2004***). The fact that interevent times for biofilm sloughing also seem to follow a Gamma distribution may point towards specific physical mechanisms (***Kumar et al., 2020***), which could be used in future works to better understand the physics of sloughing. One interesting perspective of this work is also to assess the universality of these distributions across microorganisms and whether we could define classes of bacteria with specific signatures on the stochastic process. With the same idea, we could further evaluate the impact of ecological interactions in multispecies biofilm or the effect of various molecules, such as biocides, on the sloughing dynamics.

## Material and Methods

### Bacteria and cultures

Experiments were performed using *Pseudomonas aeruginosa* PAO1 GFP (ATCC 15692GFP) strain, along with PAO1 GFP $\Delta psl D$ and $\Delta pel F$ mutants obtained from ***Colvin et al.*** (***2011***, 2012) and built by non-polar deletion through allelic replacement of *pslD* and *pelF* operon and harbor pMRP9-1 plasmid expressing GFP. Bacteria were subcultured and grown in brain heart infusion (Sigma Aldrich, Saint-Quentin-Fallavier, France). Cultures were prepared from -80°C frozen aliquots spread on tryptic soy agar plate (Sigma Aldrich, Saint-Quentin-Fallavier, France) supplemented with $300$ µg/mL of ampicillin (Sigma Aldrich) then incubated at 30°C during 24 h. Liquid cultures were prepared from the second subcluture on tryptic soy agar by spreading a 24 hours single colony diluted in brain heart infusion media supplemented with 300 µg/mL of ampicillin. $1X$ concentrated BHI media was prepared by dissolving $37\,g$ of commercial powder in demineralized water and autoclaved with a liquid cycle (121° C for 15 minutes). $0.2X$ concentrated BHI media was obtained by dissolving $7.4\,g$ while a third $1X$ solution was supplemented by $8\,g/L$ of D-Glucose (Sigma Aldrich).

### Microfabrication

Microchannels were fabricated using standard soft lithography techniques. Microchannel molds were prepared by depositing 100 µm SUEX sheets on a silicium wafer via photolithography. The negative mold was cleaned by isopropanol and silanized with trichloromethylsilane (Sigma Aldrich). Square cross-section channels had dimensions of 100 µm height by 100 µm width and 20 mm length. The chips were prepared with a 10% wt/wt cross-linking agent in the polydimethylsiloxane solution (Sylgard 184 Silicone Elastomer Kit, Dow Corning). PDMS was cleaned with isopropanol at 80 °C for 30 minutes and plasma-bonded to a clean glass coverslide.

### Inoculation and flow experiments

BHI suspensions were adjusted at optical density at $OD_{620\,nm}$= 0.2 ($10^8\,CFU/mL$ ) and inoculated inside the microchannels from the outlet, up to approximately $^3/_4$ of the channel length in order to keep a clean inlet. The system was let at room temperature (25°C) for 3h under static conditions. Flow experiments were then performed at $0.02, 0.2, 2, 20$ and $200\ \mu L/min$ constant flow rates for 72h in the microchannels at room temperature. For the experiments at $0.2, 2, 20$ and $200\ \mu L/min$, the fluidic system was based on a sterile culture medium reservoir pressurized by a pressure controller (Fluigent FlowEZ) and connected with a flow rate controller (Fluigent Flow unit). The flow rate was maintained constant by using a controller with a feedback loop adjusting the pressure in the liquid reservoir. The reservoir was connected to the chip using Tygon tubing (Saint Gobain Life Sciences Tygon™ ND 100-80) of 0.52 mm internal diameter and 1.52 mm external diameter, along with PEEK tubing (Cytiva Akta pure) with 0.25 mm inner diameter adapters for flow rate controller. The waste container was also pressurized by another independent pressure controller to reduce air bubble formation in the inlet part. For the experiments at $0.02\ \mu L/min$, we used an Harvard Phd2000 syringe pump for the flow.

### UVC irradiation

The biofilm is constrained in a part of the microchannel using UVC irradiation directly through the PDMS of the microfluidic chips, thus reducing contamination risk and avoiding unwanted progression/growth of *P. aeruginosa* in the inlet and tubing for several days of experiment (***Ramos et al., 2023***). This eliminates parasitic consumption of nutrients in various parts of the fluidic system and maintain a controlled boundary condition with a fixed concentration of nutrients at the inlet of our zone of interest.

To this end, the inlet and outlet of the microchannels were exposed to UVC light by a system of UVC LEDs (***Ramos et al., 2023***). The system consists of a 3D printed part called the guide carrying in its backside a PCB with a LED light source that delivers UV-C light of 1W power. The light

beam follows a straight trajectory until a 45° mirror positioned in the front side of the guide, which reflects the light parallel to the PDMS chip and irradiate it. UVC guides were positioned in both sides of the PDMS microchannel and separated by a 1.2 cm distance to keep a central area unexposed. UVC power is measured by a radiometer after mirror reflection and delivers a power of $200\,mW/m^2$ equivalent to $2\,mJ/cm^2$. The guide is elevated to fit with the PDMS chip dimensions and contains a barrier located in the front side that blocks the diffusion of light through the PDMS polymer in the horizontal direction.

### Mass spectrometry analysis

Mass spectrometry analysis was performed on a Thermo Scientific Q Exactive Focus Orbitrap LC-MS/MS system connected to a LC device Thermo Scientific Vanquish UPLC system with PDA detection. Analytical separations were performed on a 150 x 2.1 mm Thermo Hypersyl Gold C18 column (1.9 µm) using an MeCN/H2O 1% formic acid gradient. Data were captured in full MS scan mode and processed using Chromeleon 7 software.

### Imaging for the biofilm experiment

Bacterial development was imaged for a period of 72 hours with a timestep of 30 minutes at 25°C on an inverted microscope (Ti-2E, Nikon) using a digital camera (back-illuminated PCO edge). Time-lapse images were acquired using brightfield and fluorescence microscopy (Sola light source 10% intensity with 30 ms exposure with $500\,nm$ excitation and $513\,nm$ emission combined with (FITC filter). Images were obtained with a focal plan at the glass/liquid interface. These images had dimensions of 30086 x 154 pixels obtained after multi position scanning using automatic Nikon platform and assembled by Nikon NIS software of single images with $0.65$ µm/pixel using a 10X magnification Nikon objective (NA = 0.3).

### Image analysis for the biofilm distribution in the longitudinal direction

Fluorescence images were loaded as a matrix (30086 x 154) in MATLAB (MathWorks). For each time acquisition, the signal was first integrated in the radial direction to obtain a mean distribution in the longitudinal direction. In plotting curves to analyze the effect of nutrients, all timepoints were then averaged to obtain one dimensional curves of the mean longitudinal profile. For kymographs, one dimensional curves for each time point were stacked together to describe the spatio-temporal dynamics. The intensity values were normalized to the maximum values of each replicate over all times. For each flow and nutrient condition, three biological replicates were performed.

### Image analysis for the biofilm segmentation

To estimate changes in channel colonization, GFP images were binarized using a machine learning software (Ilastik) (***Berg et al., 2019***). Images were pre-treated with imageJ (***Schneider et al., 2012***) by normalizing all pixel values between 0 and 65535 grayscale levels. In Ilastik, biofilm structures were first differentiated from the empty flow path using pixel-level manual labeling during pixel classification where visible patches of biofilm and empty channel were annotated manually by mouse cursor. Pixel classification workflow employs a Random Forest classifier, known for its generalization properties. Several samples of biofilm and background images were used to train the classifier by annotating pixels with corresponding labels, allowing the algorithm to learn and make predictions in real-time. The chosen features were color, intensity, edges, and texture. The generated probability maps indicating the likelihood of each class at every pixel were used for the object classification and were thresholded at a value of 0.6 with no size filter. Thresholding is a process involved in converting continuous probability maps generated from pixel classification into binary segmentation images by setting a threshold, where pixels above the threshold are classified as belonging to an object. The size, intensity, position and convexity of the biofilm objects was exported in .cvs format and further analysed in matlab. Volumic fraction of biofilm in microchannel

was calculated from the sum of the size of segmented objects divided by the interest growth area (non UVC irradiated central part of microchannel).

### Initial adhesion

Separate experiments were performed to study the behavior of cells in the initial phases of attachment in order to increase spatial and temporal resolution. Liquid cultures were prepared following the same protocol as described previously (). Sterile $1\times$ concentrated BHI culture medium supplemented by $300\,\mu g/mL$ of ampicillin was flowed under constant flow rate ($Q = 0.2\ \mu L/min$, $2\ \mu L/min$ and $20\ \mu L/min$) after 3 hours under static conditions at 26° C.

Images were obtained with a 40× Nikon objective (NA = 0.95) using a differential interference contrast (DIC) brightfield with 2 minutes per frame during 3.5 Hours. Replicates were obtained by imaging four positions per channel and each condition was performed in two distinct channels forming two distinct biological replicates to obtain n = 8 replicates by condition ($Q = 0.2\ \mu L/min$, $2\ \mu L/min$ and $20\ \mu L/min$). The images were further segmented using Ilastik with the same parameters as described before and single cells were selected as objects with an area higher than $20\ \mu m^2$ to avoid counting dust particles and artefacts that could be considered as distinct objects by Ilastik. The doubling time was calculated in the window between 0 and 3.5 hours by a a linear fitting of the logarithm of the number of cells. The slope was used to estimate growth rate and doubling time. Cell count was calculated from image segmentation of four positions in two channels to generate 8 replicates by condition (n= 8) for ($Q = 0.2\ \mu L/min$, $2\ \mu L/min$ and $20\ \mu L/min$).

### Wavelet analysis

Time series of the pressure data were investigated with a wavelet analysis to identify temporal variations of spectral power (***Torrence and Compo, 1998***). Wavelet analysis was carried out using a Morlet wavelet, the product of a sinusoidal wave and a Gaussian envelope, with a frequency parameter of 6 and scale width of 300. We then applied a continuous wavelet transform (CWT) results which gives wave power coefficients dependent on the scale or period and the time, as well as a cone of influence (COI), where edge effects become important. The time series were zero-padded to reduce the edge errors. The cone of influence was removed from the scalograms in Fig 3.

### Data analysis for the calculation of the hydraulic resistance and volume fraction

Recorded pressure fluctuations in the reservoir were converted to hydraulic resistance in the 10 mm zone between UVC LEDs where biofilm develops. We write the difference between the two pressure reservoirs (one at the inlet and one at the outlet) as $\Delta P_{\text{res}}$ and express it as

$$\Delta P_{\text{res}}(t) = \left( \sum_i R_i + R(t) \right) Q$$

with $Q$ the imposed flow rate, $\sum_i R_i$ the sum of the hydraulic resistance of the different part of the hydraulic network and $R(t)$ the hydraulic resistance of the the 10 mm zone between UVC LEDs. To estimate $R(t)$, we evaluated $\sum_i R_i$ from the mean value of $\Delta P_{\text{res}}$, which we write $\overline{\Delta P}_{\text{res}}$, over a few hours of the experiment where biofilm growth is not yet observable. We then use

$$\sum_i R_i = \frac{\overline{\Delta P}_{\text{res}}}{Q} - R(t=0),$$

which yields

$$\frac{R(t)}{R(t=0)} = 1 + \frac{\Delta P_{\text{res}}(t) - \overline{\Delta P}_{\text{res}}}{Q\ R(t=0)},$$

| $Q$ | $a$ | $b$ | $\mu$ | $\sigma$ |
|---|---|---|---|---|
| $0.2\ \mu L/min$ | 3.71 | $7.28 \times 10^{-2}$ | −5.19 | 1.28 |
| $2\ \mu L/min$ | 3.51 | $8.90 \times 10^{-2}$ | −5.07 | 1.29 |
| $20\ \mu L/min$ | 1.53 | $2.50 \times 10^{-1}$ | −3.90 | 1.34 |

**Table 2.** Values obtained from direct fitting of the experimental data

with $R(t=0)$ in the square cross-section of size $h_0 = 100\ \mu m$ that can be estimated as

$$R(t=0) \simeq \frac{12\eta L}{1 - 0.917 \times 0.63} \frac{1}{h^4}$$

with $\eta$ the viscosity of the culture medium at 25°C, $L = 10\ mm$ the length of the channel and $h$ the width/height of the channel. Since we considered $\overline{\Delta P}_{\text{res}}$ for the normalization, and because the low pressure signal is relatively noisy at the beginning, we also only use the part of the signal for which $\frac{R(t)}{R(t=0)} \geq 1$ – it is a important, for instance, to obtain non-negative volume fractions of biofilm that are only the result of the initial noise. Upon assuming that the biofilm forms a uniform layer on the sides of the channel (see schematics in Fig S1), we also have

$$\frac{R(t)}{R(t=0)} = \left(\frac{h}{h-2b}\right)^4,$$

with $b$ the thickness of the biofilm layer. The volume fraction of biofilm is $\phi = 1 - \left(\frac{h-2b}{h}\right)^2$ so that

$$\phi = 1 - \sqrt{\frac{R(t=0)}{R(t)}}.$$

## Frequency analysis

Welch power spectral analysis (***Welch, 1967***) of the pressure signal was carried out by dividing the time signal into smaller segments, calculating their periodogram and finally averaging accross the frequencies, resulting in a power spectral density (PSD) estimate. This method allows for PSD estimate that is less noisy than usual periodograms. Here, we used the Matlab tool pwelch to estimate the PSD using hanning window with an overlap of 50%. A linear fit was then applied on the interval in the low frequency range.

## Construction of the probability density functions for jumps and fits

Volume fraction data were processed using a homemade Matlab code. Each dataset was first subsampled by keeping only 1 in 150 points. The subsampled signal was then differentiated and only negative values corresponding to detachment events were conserved. Jumps were then identified through the selection of local maxima. For each flow rate, all the values for the times between two successive jumps and the relative amplitude of the jumps – amplitude of the jump relative to the value of the volume fraction just before the jump – for the different replicates were aggregated to construct the distributions.

Gamma distributions were then fitted to the experimental data for the times between successive jumps and lognormal distributions were used for the amplitude of the jumps. Values for the different parameters are summarized in Table.2.

## Numerical simulation of the stochastic process

Here we describe how we simulated the evolution of the volume fraction $\phi$, solving

$$d\phi_t = \phi_t \left(1 - \frac{1-\phi_{\max}}{1-\phi_t}\right) dt - \phi_{t^-} dN_t. \tag{10}$$

The simulation was done using a homemade Matlab code. For each case, based on the previously calculated distributions, we first generated two sets of random numbers corresponding to the times between successive jumps and to the relative amplitude of the jumps – therefore allowing us to completely determine the jump process, $N$. We then simply solved the ordinary differential equation

$$\dot{\phi} = \phi \left( 1 - \frac{1 - \phi_{\max}}{1 - \phi} \right), \tag{11}$$

between jumps using the Matlab solve ode45. Upon reaching a jump, the simulation was stopped and the jump implemented, before proceeding to treating the next interval.

### Comsol flow simulations

Flow simulation was performed using a finite element approach in Comsol v6.1. The channel was treated as a rectangle of $850\,\mu m$ length by $100\,\mu m$ width. Biofilm, as shown in white in Fig 6, was added from a segmentation of real experimental images. We then solved incompressible Stokes flow with no-slip/no-penetration boundary conditions on the solid and on the biofilm surface. The inlet condition was an imposed velocity, while the outlet was an imposed pressure.

## Acknowledgments

This work is part of a project that has received funding from the European Research Council (ERC) under the European Union's Horizon 2020 research and innovation programme (grant agreement no 803074). This work was partially supported by the LAAS-CNRS micro and nanotechnologies platform, a member of the French Renatech network. We thank the entire BEBOP team for daily interactions and assistance; Julien Lefort and Emmanuel Libert for their technical support; Terence Desclaux for the introduction to wavelet analysis; Matthew R. Parsek and Maria Zori for providing the Pel and Psl mutants; and Laure Latapie for her support with mass spectrometry.

## References

**Alvarez-Ortega C**, Harwood CS. Responses of Pseudomonas Aeruginosa to Low Oxygen Indicate That Growth in the Cystic Fibrosis Lung Is by Aerobic Respiration. Molecular microbiology. 2007 Jul; 65(1):153–165. doi: 10.1111/j.1365-2958.2007.05772.x.

**Arat S**, Bullerjahn GS, Laubenbacher R. A Network Biology Approach to Denitrification in Pseudomonas Aeruginosa. PLoS ONE. 2015 Feb; 10(2):e0118235. doi: 10.1371/journal.pone.0118235.

**Aslam M**, Ahmad R, Kim J. Recent Developments in Biofouling Control in Membrane Bioreactors for Domestic Wastewater Treatment. Separation and Purification Technology. 2018 Nov; 206:297–315. doi: 10.1016/j.seppur.2018.06.004.

**Bartberger MD**, Liu W, Ford E, Miranda KM, Switzer C, Fukuto JM, Farmer PJ, Wink DA, Houk KN. The Reduction Potential of Nitric Oxide (NO) and Its Importance to NO Biochemistry. Proceedings of the National Academy of Sciences. 2002 Aug; 99(17):10958–10963. doi: 10.1073/pnas.162095599.

**Battin TJ**, Besemer K, Bengtsson MM, Romani AM, Packmann AI. The Ecology and Biogeochemistry of Stream Biofilms. Nature Reviews Microbiology. 2016 Apr; 14(4):251–263. doi: 10.1038/nrmicro.2016.15.

**Berg S**, Kutra D, Kroeger T, Straehle CN, Kausler BX, Haubold C, Schiegg M, Ales J, Beier T, Rudy M, Eren K, Cervantes JI, Xu B, Beuttenmueller F, Wolny A, Zhang C, Koethe U, Hamprecht FA, Kreshuk A. Ilastik: Interactive Machine Learning for (Bio)Image Analysis. Nature Methods. 2019 Dec; 16(12):1226–1232. doi: 10.1038/s41592-019-0582-9.

**Besemer K**, Singer G, Limberger R, Chlup AK, Hochedlinger G, Hödl I, Baranyi C, Battin TJ. Biophysical Controls on Community Succession in Stream Biofilms. Applied and Environmental Microbiology. 2007 Aug; 73(15):4966–4974. doi: 10.1128/AEM.00588-07.

**Bixler G**, Bhushan B. Review Article: Biofouling: Lessons from Nature. Philosophical transactions Series A, Mathematical, physical, and engineering sciences. 2012 May; 370:2381–417. doi: 10.1098/rsta.2011.0502.

**Bohn A**, Zippel B, Almeida JS, Xavier JB. Stochastic modeling for characterisation of biofilm development with discrete detachment events (sloughing). Water Science and Technology: A Journal of the International Association on Water Pollution Research. 2007; 55(8-9):257–264. doi: 10.2166/wst.2007.266.

**Boles BR**, Thoendel M, Singh PK. Rhamnolipids mediate detachment of Pseudomonas aeruginosa from biofilms. Molecular Microbiology. 2005; 57(5):1210–1223. https://onlinelibrary.wiley.com/doi/abs/10.1111/j.1365-2958.2005.04743.x, doi: 10.1111/j.1365-2958.2005.04743.x, _eprint: https://onlinelibrary.wiley.com/doi/pdf/10.1111/j.1365-2958.2005.04743.x.

**Bottero S**, Storck T, Heimovaara TJ, Van Loosdrecht MCM, Enzien MV, Picioreanu C. Biofilm Development and the Dynamics of Preferential Flow Paths in Porous Media. Biofouling. 2013 Oct; 29(9):1069–1086. doi: 10.1080/08927014.2013.828284.

**Bruus H**. Theoretical Microfluidics. OUP Oxford; 2008.

**Busscher HJ**, van der Mei HC. Microbial Adhesion in Flow Displacement Systems. Clinical Microbiology Reviews. 2006 Jan; 19(1):127–141. doi: 10.1128/CMR.19.1.127-141.2006.

**Characklis WG**, Trulear MG, Bryers JD, Zelver N. Dynamics of Biofilm Processes: Methods. Water Research. 1982 Jan; 16(7):1207–1216. doi: 10.1016/0043-1354(82)90139-7.

**Chen MJ**, Zhang Z, Bott TR. Direct measurement of the adhesive strength of biofilms in pipes by micromanipulation. Biotechnology Techniques. 1998 Dec; 12(12):875–880. https://doi.org/10.1023/A:1008805326385, doi: 10.1023/A:1008805326385.

**Colón-González M**, Méndez-Ortiz MM, Membrillo-Hernández J. Anaerobic Growth Does Not Support Biofilm Formation in Escherichia Coli K-12. Research in Microbiology. 2004 Sep; 155(7):514–521. doi: 10.1016/j.resmic.2004.03.004.

**Colvin KM**, Gordon VD, Murakami K, Borlee BR, Wozniak DJ, Wong GCL, Parsek MR. The Pel Polysaccharide Can Serve a Structural and Protective Role in the Biofilm Matrix of Pseudomonas Aeruginosa. PLoS Pathogens. 2011 Jan; 7(1):e1001264. doi: 10.1371/journal.ppat.1001264.

**Colvin KM**, Irie Y, Tart CS, Urbano R, Whitney JC, Ryder C, Howell PL, Wozniak DJ, Parsek MR. The Pel and Psl Polysaccharides Provide Pseudomonas Aeruginosa Structural Redundancy within the Biofilm Matrix. Environmental microbiology. 2012 Aug; 14(8):10.1111/j.1462–2920.2011.02657.x. doi: 10.1111/j.1462-2920.2011.02657.x.

**Conrad JC**, Poling-Skutvik R. Confined Flow: Consequences and Implications for Bacteria and Biofilms. Annual Review of Chemical and Biomolecular Engineering. 2018; 9(1):175–200. https://doi.org/10.1146/annurev-chembioeng-060817-084006, doi: 10.1146/annurev-chembioeng-060817-084006, _eprint: https://doi.org/10.1146/annurev-chembioeng-060817-084006.

**Corral Á**. Long-Term Clustering, Scaling, and Universality in the Temporal Occurrence of Earthquakes. Physical Review Letters. 2004 Mar; 92(10):108501. doi: 10.1103/PhysRevLett.92.108501.

**Costerton JW**, Lewandowski Z, Caldwell DE, Korber DR, Lappin-Scott HM. Microbial Biofilms. Annual Review of Microbiology. 1995; 49:711–745. doi: 10.1146/annurev.mi.49.100195.003431.

**Cowle MW**, Babatunde AO, Rauen WB, Bockelmann-Evans BN, Barton AF. Biofilm Development in Water Distribution and Drainage Systems: Dynamics and Implications for Hydraulic Efficiency. Environmental Technology Reviews. 2014 Jan; 3(1):31–47. doi: 10.1080/09593330.2014.923517.

**Coyte KZ**, Tabuteau H, Gaffney EA, Foster KR, Durham WM. Microbial Competition in Porous Environments Can Select against Rapid Biofilm Growth. Proceedings of the National Academy of Sciences. 2017 Jan; 114(2):E161–E170. doi: 10.1073/pnas.1525228113.

**Cunningham AB**, Characklis WG, Abedeen F, Crawford D. Influence of biofilm accumulation on porous media hydrodynamics. Environmental Science & Technology. 1991 Jul; 25(7):1305–1311. https://doi.org/10.1021/es00019a013, doi: 10.1021/es00019a013, publisher: American Chemical Society.

**Desmond P**, Huisman KT, Sanawar H, Farhat NM, Traber J, Fridjonsson EO, Johns ML, Flemming HC, Picioreanu C, Vrouwenvelder JS. Controlling the hydraulic resistance of membrane biofilms by engineering biofilm physical structure. Water Research. 2022 Feb; 210:118031. https://www.sciencedirect.com/science/article/pii/S0043135421012252, doi: 10.1016/j.watres.2021.118031.

**Drescher K**, Shen Y, Bassler BL, Stone HA. Biofilm Streamers Cause Catastrophic Disruption of Flow with Consequences for Environmental and Medical Systems. Proceedings of the National Academy of Sciences. 2013 Mar; 110(11):4345–4350. doi: 10.1073/pnas.1300321110.

**Duddu R**, Chopp DL, Moran B. A Two-dimensional Continuum Model of Biofilm Growth Incorporating Fluid Flow and Shear Stress Based Detachment. Biotechnology and Bioengineering. 2009 May; 103(1):92–104. doi: 10.1002/bit.22233.

**Dufrêne YF**, Persat A. Mechanomicrobiology: How Bacteria Sense and Respond to Forces. Nature Reviews Microbiology. 2020 Apr; 18(4):227–240. doi: 10.1038/s41579-019-0314-2.

**Emerenini BO**, Hense BA, Kuttler C, Eberl HJ. A Mathematical Model of Quorum Sensing Induced Biofilm Detachment. PLOS ONE. 21 juil 2015; 10(7):e0132385. doi: 10.1371/journal.pone.0132385.

**Emge P**, Moeller J, Jang H, Rusconi R, Yawata Y, Stocker R, Vogel V. Resilience of Bacterial Quorum Sensing against Fluid Flow. Scientific Reports. 2016 Sep; 6(1):33115. doi: 10.1038/srep33115.

**Flemming HC**, Wingender J. The Biofilm Matrix. Nature Reviews Microbiology. 2010 Sep; 8(9):623–633. doi: 10.1038/nrmicro2415.

**Flemming HC**, Wingender J, Szewzyk U, Steinberg P, Rice SA, Kjelleberg S. Biofilms: An Emergent Form of Bacterial Life. Nature Reviews Microbiology. 2016 Sep; 14(9):563–575. doi: 10.1038/nrmicro.2016.94.

**Folsom JP**, Richards L, Pitts B, Roe F, Ehrlich GD, Parker A, Mazurie A, Stewart PS. Physiology of Pseudomonas Aeruginosa in Biofilms as Revealed by Transcriptome Analysis. BMC Microbiology. 2010 Nov; 10:294. doi: 10.1186/1471-2180-10-294.

**García S**, Trueba A. Fouling in Heat Exchangers. In: Bhattacharya S, Moghimi Ardekani M, Biswas R, C Mehta R, editors. *Inverse Heat Conduction and Heat Exchangers* IntechOpen; 2020.doi: 10.5772/intechopen.88079.

**Gloag ES**, Fabbri S, Wozniak DJ, Stoodley P. Biofilm Mechanics: Implications in Infection and Survival. Biofilm. 2020 Dec; 2:100017. doi: 10.1016/j.bioflm.2019.100017.

**Guaglianone E**, Cardines R, Vuotto C, Di Rosa R, Babini V, Mastrantonio P, Donelli G. Microbial Biofilms Associated with Biliary Stent Clogging. FEMS Immunology & Medical Microbiology. 2010 Aug; 59(3):410–420. doi: 10.1111/j.1574-695X.2010.00686.x.

**Howell JA**, Atkinson B. Sloughing of microbial film in trickling filters. Water Research. 1976 Jan; 10(4):307–315. https://www.sciencedirect.com/science/article/pii/004313547690172X, doi: 10.1016/0043-1354(76)90172-X.

**Jiang Z**, Nero T, Mukherjee S, Olson R, Yan J. Searching for the Secret of Stickiness: How Biofilms Adhere to Surfaces. Frontiers in Microbiology. 2021; 12. https://www.readcube.com/articles/10.3389%2Ffmicb.2021.686793, doi: 10.3389/fmicb.2021.686793.

**Kaplan JB**. Biofilm Dispersal: Mechanisms, Clinical Implications, and Potential Therapeutic Uses. Journal of Dental Research. 2010 Mar; 89(3):205–218. doi: 10.1177/0022034509359403.

**Kim MK**, Ingremeau F, Zhao A, Bassler BL, Stone HA. Local and Global Consequences of Flow on Bacterial Quorum Sensing. Nature Microbiology. 2016 Jan; 1(1):15005. doi: 10.1038/nmicrobiol.2015.5.

**Körstgens V**, Flemming HC, Wingender J, Borchard W. Uniaxial compression measurement device for investigation of the mechanical stability of biofilms. Journal of Microbiological Methods. 2001 Jul; 46(1):9–17. doi: 10.1016/s0167-7012(01)00248-2.

**Krsmanovic M**, Biswas D, Ali H, Kumar A, Ghosh R, Dickerson AK. Hydrodynamics and Surface Properties Influence Biofilm Proliferation. Advances in Colloid and Interface Science. 2021; 288:102336. doi: 10.1016/j.cis.2020.102336.

**Kryachko Y**. Novel Approaches to Microbial Enhancement of Oil Recovery. Journal of Biotechnology. 2018 Jan; 266:118–123. doi: 10.1016/j.jbiotec.2017.12.019.

**Kumar P**, Korkolis E, Benzi R, Denisov D, Niemeijer A, Schall P, Toschi F, Trampert J. On Interevent Time Distributions of Avalanche Dynamics. Scientific Reports. 2020 Jan; 10(1):626. doi: 10.1038/s41598-019-56764-6.

**Kurz DL**, Secchi E, Carrillo FJ, Bourg IC, Stocker R, Jimenez-Martinez J. Competition between Growth and Shear Stress Drives Intermittency in Preferential Flow Paths in Porous Medium Biofilms. Proceedings of the National Academy of Sciences. 2022 Jul; 119(30):e2122202119. doi: 10.1073/pnas.2122202119.

**Lau PCY**, Dutcher JR, Beveridge TJ, Lam JS. Absolute Quantitation of Bacterial Biofilm Adhesion and Viscoelasticity by Microbead Force Spectroscopy. Biophysical Journal. 2009 Apr; 96(7):2935–2948. https://www.sciencedirect.com/science/article/pii/S0006349509004226, doi: 10.1016/j.bpj.2008.12.3943.

**Lee SH**, Secchi E, Kang PK. Rapid Formation of Bioaggregates and Morphology Transition to Biofilm Streamers Induced by Pore-Throat Flows. Proceedings of the National Academy of Sciences. 2023 Apr; 120(14):e2204466120. doi: 10.1073/pnas.2204466120.

**Lennox J**, Ashe J. Biofilms as Biobarriers. The American Biology Teacher. 2009 Jan; 71(1):20–26. doi: 10.2307/27669358.

**Lewandowski Z**, Beyenal H, Stookey D. Reproducibility of biofilm processes and the meaning of steady state in biofilm reactors. Water Science and Technology: A Journal of the International Association on Water Pollution Research. 2004; 49(11-12):359–364.

**Maaß R**, Wraith M, Uhl JT, Greer JR, Dahmen KA. Slip Statistics of Dislocation Avalanches under Different Loading Modes. Physical Review E. 2015 Apr; 91(4):042403. doi: 10.1103/PhysRevE.91.042403.

**Mukherjee S**, Bassler BL. Bacterial Quorum Sensing in Complex and Dynamically Changing Environments. Nature Reviews Microbiology. 2019 Jun; 17(6):371–382. doi: 10.1038/s41579-019-0186-5.

**Ohashi A**, Harada H. A novel concept for evaluation of biofilm adhesion strength by applying tensile force and shear force. Water Science and Technology. 1996 Jan; 34(5):201–211. https://www.sciencedirect.com/science/article/pii/0273122396006476, doi: 10.1016/0273-1223(96)00647-6.

**Paul E**, Ochoa JC, Pechaud Y, Liu Y, Liné A. Effect of Shear Stress and Growth Conditions on Detachment and Physical Properties of Biofilms. Water Research. 2012 Nov; 46(17):5499–5508. doi: 10.1016/j.watres.2012.07.029.

**Peterson BW**, He Y, Ren Y, Zerdoum A, Matthew R Libera, Sharma PK, van Winkelhoff AJ, Neut D, Stoodley P, van der Mei HC, Busscher HJ. Viscoelasticity of Biofilms and Their Recalcitrance to Mechanical and Chemical Challenges. FEMS microbiology reviews. 2015 Mar; 39(2):234–245. doi: 10.1093/femsre/fuu008.

**Picioreanu C**, Van Loosdrecht MC, Heijnen JJ. Effect of Diffusive and Convective Substrate Transport on Biofilm Structure Formation: A Two-Dimensional Modeling Study. Biotechnology and Bioengineering. 2000 Sep; 69(5):504–515. doi: 10.1002/1097-0290(20000905)69:5<504::aid-bit5>3.0.co;2-s.

**Ramos G**, Toulouze C, Rima M, Liot O, Duru P, Davit Y. Ultraviolet Control of Bacterial Biofilms in Microfluidic Chips. Biomicrofluidics. 2023 Mar; 17(2):024107. doi: 10.1063/5.0135722.

**Rasamiravaka T**, Labtani Q, Duez P, El Jaziri M. The Formation of Biofilms by *Pseudomonas Aeruginosa* : A Review of the Natural and Synthetic Compounds Interfering with Control Mechanisms. BioMed Research International. 2015; 2015:1–17. doi: 10.1155/2015/759348.

**Rittman BE**. The Effect of Shear Stress on Biofilm Loss Rate. Biotechnology and Bioengineering. 1982; 24(2):501–506. doi: 10.1002/bit.260240219.

**Rittmann BE**. The significance of biofilms in porous media. Water Resources Research. 1993; 29(7):2195–2202. https://onlinelibrary.wiley.com/doi/abs/10.1029/93WR00611, doi: 10.1029/93WR00611.

**Rodesney CA**, Roman B, Dhamani N, Cooley BJ, Katira P, Touhami A, Gordon VD. Mechanosensing of Shear by Pseudomonas Aeruginosa Leads to Increased Levels of the Cyclic-Di-GMP Signal Initiating Biofilm Development. Proceedings of the National Academy of Sciences. 2017 Jun; 114(23):5906–5911. doi: 10.1073/pnas.1703255114.

**Rossy T**, Nadell CD, Persat A. Cellular Advective-Diffusion Drives the Emergence of Bacterial Surface Colonization Patterns and Heterogeneity. Nature Communications. 2019 Jun; 10(1):2471. doi: 10.1038/s41467-019-10469-6.

**Rusconi R**, Lecuyer S, Autrusson N, Guglielmini L, Stone HA. Secondary Flow as a Mechanism for the Formation of Biofilm Streamers. Biophysical Journal. 2011 Mar; 100(6):1392–1399. doi: 10.1016/j.bpj.2011.01.065.

**Ryder C**, Byrd M, Wozniak DJ. Role of Polysaccharides in Pseudomonas Aeruginosa Biofilm Development. Current Opinion in Microbiology. 2007 Dec; 10(6):644–648. doi: 10.1016/j.mib.2007.09.010.

**Sabra W**, Kim EJ, Zeng AP. Physiological Responses of Pseudomonas Aeruginosa PAO1 to Oxidative Stress in Controlled Microaerobic and Aerobic Cultures. Microbiology (Reading, England). 2002 Oct; 148(Pt 10):3195–3202. doi: 10.1099/00221287-148-10-3195.

**Sampedro I**, Parales RE, Krell T, Hill JE. *Pseudomonas* Chemotaxis. FEMS Microbiology Reviews. 2014 Oct; p. n/a–n/a. doi: 10.1111/1574-6976.12081, chemotaxis Positive and negative.

**Sanfilippo JE**, Lorestani A, Koch MD, Bratton BP, Siryaporn A, Stone HA, Gitai Z. Microfluidic-Based Transcriptomics Reveal Force-Independent Bacterial Rheosensing. Nature Microbiology. 2019 May; 4(8):1274–1281. doi: 10.1038/s41564-019-0455-0.

**Schneider CA**, Rasband WS, Eliceiri KW. NIH Image to ImageJ: 25 Years of Image Analysis. Nature methods. 2012 Jul; 9(7):671–675.

**Sen R**. Biotechnology in Petroleum Recovery: The Microbial EOR. Progress in Energy and Combustion Science. 2008 Dec; 34(6):714–724. doi: 10.1016/j.pecs.2008.05.001.

**Sharp RR**, Stoodley P, Adgie M, Gerlach R, Cunningham A. Visualization and Characterization of Dynamic Patterns of Flow, Growth and Activity of Biofilms Growing in Porous Media. Water Science and Technology. 2005 Oct; 52(7):85–90. doi: 10.2166/wst.2005.0185.

**Singh R**, Paul D, Jain RK. Biofilms: Implications in Bioremediation. Trends in Microbiology. 2006 Sep; 14(9):389–397. doi: 10.1016/j.tim.2006.07.001.

**Stewart TL**, Fogler HS. Biomass Plug Development and Propagation in Porous Media. Biotechnology and Bioengineering. 2001 Feb; 72(3):353–363. doi: 10.1002/1097-0290(20010205)72:3<353::AID-BIT13>3.0.CO;2-U.

**Stewart TL**, Scott Fogler H. Pore-scale Investigation of Biomass Plug Development and Propagation in Porous Media. Biotechnology and Bioengineering. 2002 Mar; 77(5):577–588. doi: 10.1002/bit.10044.

**Stickler DJ**. Clinical Complications of Urinary Catheters Caused by Crystalline Biofilms: Something Needs to Be Done. Journal of Internal Medicine. 2014 Aug; 276(2):120–129. doi: 10.1111/joim.12220.

**Stoodley P**, Dodds I, Boyle Jd, Lappin-Scott Hm. Influence of Hydrodynamics and Nutrients on Biofilm Structure. Journal of Applied Microbiology. 1998; 85(S1):19S–28S. doi: 10.1111/j.1365-2672.1998.tb05279.x.

**Taherzadeh D**, Picioreanu C, Horn H. Mass Transfer Enhancement in Moving Biofilm Structures. Biophysical Journal. 2012 Apr; 102(7):1483–1492. doi: 10.1016/j.bpj.2012.02.033.

**Talon L**. On the Determination of a Generalized Darcy Equation for Yield Stress Fluid in Porous Media. Science Talks. 2022 Aug; 3:100042. doi: 10.1016/j.sctalk.2022.100042.

**Taylor SW**, Jaffé PR. Biofilm growth and the related changes in the physical properties of a porous medium: 1. Experimental investigation. Water Resources Research. 1990; 26(9):2153–2159. https://onlinelibrary.wiley.com/doi/abs/10.1029/WR026i009p02153, doi: 10.1029/WR026i009p02153, _eprint: https://agupubs.onlinelibrary.wiley.com/doi/pdf/10.1029/WR026i009p02153.

**Taylor SW**, Jaffé PR. Biofilm growth and the related changes in the physical properties of a porous medium: 3. Dispersivity and model verification. Water Resources Research. 1990 Sep; 26(9):2171–2180. https://agupubs.onlinelibrary.wiley.com/doi/10.1029/WR026i009p02171, doi: 10.1029/WR026i009p02171.

**Taylor SW**, Jaffé PR. Substrate and biomass transport in a porous medium. Water Resources Research. 1990 Sep; 26(9):2181–2194. https://agupubs.onlinelibrary.wiley.com/doi/10.1029/WR026i009p02181, doi: 10.1029/WR026i009p02181.

**Taylor SW**, Milly PCD, Jaffé PR. Biofilm growth and the related changes in the physical properties of a porous medium: 2. Permeability. Water Resources Research. 1990 Sep; 26(9):2161–2169. https://agupubs.onlinelibrary.wiley.com/doi/10.1029/WR026i009p02161, doi: 10.1029/WR026i009p02161.

**Telgmann U**, Horn H, Morgenroth E. Influence of Growth History on Sloughing and Erosion from Biofilms. Water Research. 2004 Oct; 38(17):3671–3684. doi: 10.1016/j.watres.2004.05.020.

**Thomen P**, Robert J, Monmeyran A, Bitbol AF, Douarche C, Henry N. Bacterial Biofilm under Flow: First a Physical Struggle to Stay, Then a Matter of Breathing. PLoS ONE. 2017 Apr; 12(4):e0175197. doi: 10.1371/journal.pone.0175197.

**Torrence C**, Compo GP. A Practical Guide to Wavelet Analysis. Bulletin of the American Meteorological Society. 1998 Jan; 79(1):61–78. doi: 10.1175/1520-0477(1998)079<0061:APGTWA>2.0.CO;2.

**Vandevivere P**, Baveye P. Effect of bacterial extracellular polymers on the saturated hydraulic conductivity of sand columns. Applied and Environmental Microbiology. 1992 May; 58(5):1690–1698. doi: 10.1128/aem.58.5.1690-1698.1992.

**Vandevivere P**, Baveye P. Saturated Hydraulic Conductivity Reduction Caused by Aerobic Bacteria in Sand Columns. Soil Science Society of America Journal. 1992 Jan; 56:1–13. doi: 10.2136/sssaj1992.03615995005600010001x.

**Verran J**. Biofouling in Food Processing: Biofilm or Biotransfer Potential. Food and Bioproducts Processing. 2002 Dec; 80(4):292–298. doi: 10.1205/096030802321154808.

**Wagner M**, Manz B, Volke F, Neu TR, Horn H. Online Assessment of Biofilm Development, Sloughing and Forced Detachment in Tube Reactor by Means of Magnetic Resonance Microscopy. Biotechnology and Bioengineering. 2010 May; 107(1):172–181. doi: 10.1002/bit.22784.

**Wang S**, Zhu H, Zheng G, Dong F, Liu C. Dynamic Changes in Biofilm Structures under Dynamic Flow Conditions. Applied and Environmental Microbiology. 2022 Oct; 88(22):e01072–22. doi: 10.1128/aem.01072-22.

**Welch P**. The Use of Fast Fourier Transform for the Estimation of Power Spectra: A Method Based on Time Averaging over Short, Modified Periodograms. IEEE Transactions on Audio and Electroacoustics. 1967 Jun; 15(2):70–73. doi: 10.1109/TAU.1967.1161901.

**Wilson S**, Hamilton MA, Hamilton GC, Schumann MR, Stoodley P. Statistical Quantification of Detachment Rates and Size Distributions of Cell Clumps from Wild-Type (PAO1) and Cell Signaling Mutant (JP1) *Pseudomonas Aeruginosa* Biofilms. Applied and Environmental Microbiology. 2004 Oct; 70(10):5847–5852. doi: 10.1128/AEM.70.10.5847-5852.2004.